# Untargeted Pixel-by-Pixel Imaging of Metabolite Ratio Pairs as a Novel Tool for Biomedical Discovery in Mass Spectrometry Imaging

Huiyong Cheng[1], Dawson Miller[1], Nneka Southwell[2], Paola Porcari[3], Joshua L. Fischer[4], Isobel Taylor[1], J. Michael Salbaum[5], Claudia Kappen[5], Fenghua Hu[6], Cha Yang[6], Kayvan R. Keshari[3], Steven S. Gross[1], Marilena D'Aurelio[2], and Qiuying Chen[1*]

[1]Department of Pharmacology and [2]Brain and Mind Research Institute, Weill Cornell Medicine, New York, NY 10021

[3]Memorial Sloan Kettering Cancer Center, New York, NY 10065

[4]Bruker Daltonics, Billerica, MA 01821

[5]Pennington Biomedical Research Center, Louisiana State University, Baton Rouge, LA 70808

[6]Cornell University, Department of Molecular Biology & Genetics, Ithaca, NY 14853-7202

*Correspondence should be addressed to:

Dr. Qiuying Chen, Weill Cornell Medicine, Department of Pharmacology, 1300 York Ave., New York, NY 10065. Phone: 212-746-6216. Email: qic2005@med.cornell.edu

**Keywords**

Metabolomics, mass spectrometry imaging; matrix-assisted laser desorption ionization mass spectrometry imaging, MALDI-MS, spatial metabolomics, metabolite ratio imaging, spatial metabotyping, tissue segmentation, metabolic pathway analysis

## Abstract

Mass spectrometry imaging (MSI) is a powerful technology used to define the spatial distribution and relative abundance of metabolites across tissue cryosections. While software packages exist for pixel-by-pixel individual metabolite and limited target pairs of ratio imaging, the research community lacks an easy computing and application tool that images any metabolite abundance ratio pairs. Importantly, recognition of correlated metabolite pairs may contribute to the discovery of unanticipated molecules in shared metabolic pathways. Here, we describe the development and implementation of an untargeted R package workflow for pixel-by-pixel ratio imaging of all metabolites detected in an MSI experiment. Considering untargeted MSI studies of murine brain and embryogenesis, we demonstrate that ratio imaging minimizes systematic data variation introduced by sample handling, markedly enhances spatial image contrast, and reveals previously unrecognized metabotype-distinct tissue regions. Furthermore, ratio imaging facilitates identification of novel regional biomarkers and provides anatomical information regarding spatial distribution of metabolite-linked biochemical pathways. The algorithm described herein is applicable to any MSI dataset containing spatial information for metabolites, peptides or proteins, offering a potent hypothesis generation tool to enhance knowledge obtained from current spatial metabolite profiling technologies.

## Abbreviations

Mass spectrometry imaging (MSI); Fourier transform ion cyclotron resonance mass spectrometry (FT-ICR-MS); Matrix-assisted laser desorption/ionization mass spectrometry imaging (MALDI-MSI); secondary ion mass spectrometry (SIMS); Desorption electrospray ionization (DESI); Cytochrome C oxidase (COX); Knockout (KO); Wildtype (WT); Genome-wide association studies (GWAS); Metabolome-wide association studies (MWAS); Phosphatidylethanolamine (PE); Phosphatidic acid (PA); Lyso-phosphatidylethanolamine (LPE); Lyso-phosphatidic acid (LPA); Cyclic phosphatidic acid (CPA); Regions of interest (ROIs), N-Acetylaspartate (NAA); N-Acetylaspartylglutamate (NAAG); NAAG synthetase (NAAGS); N-Acetyltransferase 8 (NAT8); Fatty acid (FA); Phospholipase A1 (PLA1); Phospholipase A2 (PLA2); Docosahexaenoic acid (DHA); Arachidonic acid (AA); Monounsaturated fatty acid (MUFA); Polyunsaturated fatty acids (PUFA); Fatty acid synthase (FAS); Stearoyl-CoA desaturases (SCD); Glutaminase (GLS); Asparagine synthase (ASNS); AMP deaminase (AMPD); Carnosine synthase (CARNS); Hexose kinase (HK); Glutathione (GSH); Glutathione disulfide (GSSG) Glutathione peroxidase (GPX); Principal component analysis (PCA); Partial least square discriminant analysis (PLS-DA); Receiver operating characteristic curve (ROC) curve; Variable importance in projection (VIP); Hierarchical clustering analysis (HCA); Uniform manifold approximation and projection for dimension reduction (UMAP)

## Introduction

Recent developments in mass spectrometry imaging (MSI) enable spatial mapping of the relative distribution and abundances of proteins, peptides, lipids, small molecule metabolites, drugs and elemental isotopes in heterogeneous tissue sections[1] with resolution at, or near, cellular[2]. Hence, MSI has become a promising tool in the era of spatial-omics[3-15], especially at the single cell level[16]. Matrix-assisted laser desorption and ionization (MALDI), secondary ion mass spectrometry (SIMS) and desorption electrospray ionization (DESI) are the dominant modes of ionization for MSI. Regardless of ionization method, pixel size, and knowledge of structural identity, all MSI analyses provide pixel-by-pixel relative abundances of all detected charged molecular masses. Current MSI data processing tools provide 2D or 3D image data visualization as heatmaps from normalized pixel-by-pixel data of acquired mass spectra[17-20] and are mainly limited to relative abundance data only.

Metabolite ratio imaging has been used in medical MRI spectroscopy to study metabolite distribution within tissue[21]. SIMS ratio imaging has been used in biological, material, and environmental sciences[22,23]. Additionally, targeted serum and urine metabolite ratios have aided assessment of genome-wide GWAS and MWAS association of metabolic traits by serving as proxies for enzymatic reaction rates[24-26]. Hypothesis-free testing of ratios between all possible metabolite pairs in tissue extracts analyzed by GWAS and MWAS have provided an innovative approach for discovery of new biologically meaningful molecular associations[27]. Furthermore, metabolite ratios have been used to construct large scale neural networks that improve statistical assessments and facilitate data interpretation[28]. In geographical and hyperspectral imaging, several free and commercially available software packages are available for band ratio computation and imaging. These include: 1) ENVI IDL, a geospatial imaging tool that allows ratio computation between spectral bands (https://www.nv5geospatialsoftware.com/Products/ENVI); 2) MATLAB image processing toolbox for hyperspectral imaging (https://www.mathworks.com/matlabcentral/fileexchange/50340-ratioimage); 3) Spectral Python package (Spy, https://www.spectralpython.net/); and 4) QGIS with plugins can be used for hyperspectral image analysis with a ratio between bands (https://www.qgis.org/en/site/). The above four tools can perform an individual ratio image from an input pair but may require additional programing to image ratios from the untargeted metabolite pairs in an MSI dataset (Table S1).

To fill this gap, we developed an untargeted computational R workflow to image ratios of all detected metabolites in every pixel of an MSI experiment. While individual ion abundances in spatial metabolite profiling fail to inform on metabolic pathway activity, or on the identity of metabolic intermediates contributing to these pathways, pixel-by-pixel imaging of the ratio of an enzyme's substrate to its derived product may offer an opportunity to view the distribution of functional activity for a given metabolic pathway across tissue. In this report, we use MALDI MSI data obtained from cryosections of murine embryos, brains, and a mitochondrial myopathy model of tissue derangements to demonstrate the application of ratio imaging to recognize both normal and pathology-associated regiospecific metabolic perturbations. We further show that ratio imaging minimizes systematic variations in MSI data introduced by sample handling, improves image contrast, enables anatomical mapping of metabotype heterogeneity, facilitates biomarker discovery, and reveals new spatially resolved tissue regions of interest (ROIs) that are metabolically distinct but otherwise unrecognized. Using murine embryo and hippocampus MALDI MSI data acquired at single cell spatial resolution, we showcase the potential of single cell metabolite ratios to probe metabolic enzyme activities, as well as the potential for integration with other datasets obtained using multiomic data acquisition platforms. Importantly, the algorithm for ratio imaging described should be applicable to spatial MS profiling of all sorts, including metabolites, peptides and proteins. This software package is being made available as a potent hypothesis generation

tool to enhance knowledge obtained from conventional spatial metabolite profiling analyses (https://github.com/qic2005/Untargeted-mass-spectrometry-ratio-imaging.git).

## Materials and Methods

*Sample preparation*. Brain and adipose tissues from a mitochondrial myopathy model of cytochrome c oxidase assembly factor heme A:farnesyltransferase COX10 knockout (COX10 KO) and wildtype (WT) mice and adipose were frozen in liquid nitrogen and stored at −80 °C until processing. Entire mouse decidua dissected from pregnant females at gestation day 8.5 were embedded in 2% carboxymethylcellulose, frozen in liquid nitrogen, stored at -80°C, and sectioned at 12 µm nominal thickness. Brain cryosections (n=4 per group) were cut at 10 µm and adipose at 20 µm thickness (n=3 for wildtype control and n= 4 for COX 10 KO), mounted on conductive slides coated with indium tin oxide (ITO; (Delta Technologies; cat # CB-90IN-S111) and stored at -80°C. On the day of MALDI MS data acquisition, ITO-slides with tissue sections were transferred to a vacuum chamber and dried for 30 min prior to deposition of desired matrices for imaging: N-(1-naphthyl)ethylenediamine dihydrochloride (NEDC; 10 mg/ml in 75% methanol) for murine brain and E8.5 embryos; 1,5-diaminonaphthalene (DAN, 2 mg/mL in 50% acetonitrile) for murine COX10 KO adipose tissues, and 9-aminoacridine (9AA, 5mg/ml in 85% Ethanol) for murine hippocampus. All matrices were delivered using an HTX TM-Sprayer™ (HTX Technologies LLC, NC) with optimized spraying parameters for each individual matrix. Matrix-coated tissue sections were dried in vacuum desiccator for 20 min before MALDI MSI data acquisition in negative ion detection mode.

*MALDI MSI data acquisition and processing*. MALDI MSI data were acquired at raster width of either 10 µm or 80 µm using a 7T scimaX-MRMS mass spectrometer (Bruker Daltonics, USA) equipped with a SmartBeam II laser and a MALDI source. Peak-picked MALDI-IMS data were imported into SCiLS Lab 2024b Core software (SCiLS, Bremen, Germany) for image visualization. Compound identifications were assigned based on both accurate mass (<2 ppm mass accuracy) and isotope pattern matches to free source metabolite and lipid databases, including the Human Metabolome Database (HMDB), KEGG and LIPIDMAPs. An in-house R-code developed for the programmable SCiLS Lab Application Interface (SCiLS lab API) was used for fast export of raw pixel-by-pixel metabolite and unknown mass spectral abundance data from regions of interest (ROIs) and whole tissue sections. In commercial processing software where missing values either have no value or have solid zero in abundance, we need to annotate the missing value for ratio calculation. Towards this, we first obtain the minimum abundance of a particular m/z among all pixels with detectable abundance (i.e. excluding missing values), then use 1/5 this minimum value as a threshold to annotate missing value. Pixel-by-pixel metabolite ratios between any two detected metabolites/features were calculated by applying R combination and ratio function to the annotated pixel data (see R code). Differential metabolite ratios among ROIs were visualized in R and exported as either an image or .PDF file. Figure 1 depicts a schematic workflow for metabolite ratio imaging and associated multivariate analysis among ROIs. Notably, a series of SCiLS lab API R codes for ratio imaging visualization, data analysis, UMAP segmentation are available for download on GitHub (https://github.com/qic2005/Untargeted-mass-spectrometry-ratio-imaging.git). For MSI data acquired from other non-Bruker MS imaging instruments, R codes are also available to extract pixel data directly from .imzml file, a common data format for MS imaging, using Cardinal 3.0 free-source software and the resulting pixel data can be applied for ratio imaging (Figure 1).

## Results

**1. Generation of an untargeted spectral feature list for export of pixel data to enable downstream metabolite ratio analysis.** Using SCiLS lab API, we sought to establish new data processing and analysis features for use in metabolite ratio imaging. To this end, we developed an R code that engenders fast export of raw or normalized pixel-by-pixel feature abundance data for all sections and/or regions of interest (ROIs) in an Excel.csv file format. A targeted feature list from metabolic pathways of interest can also be imported into SCiLS lab as .mir files, generated using either a Python program or a SCiLS lab feature list with manual ID annotation of peak-picked spectral data. Feature lists from multiple pathways of interest can be saved for exclusive ratio imaging of these designated pathways. Once pixel data are available, a SCiLS lab license is no longer required for metabolite ratio imaging and downstream statistical analysis, except for label and spot image generation within the SCiLS lab environment. Notably, Imaging Mass Spectrometry Markup Language (imzml) is a common data format for mass spectrometry imaging. It was developed to allow the flexible and efficient exchange of large MS imaging data between different instruments and data analysis software[29]. It contains two sets of data: the mass spectral data which is stored in a binary file (.ibd file) to ensure efficient storage and the XML metadata (.imzml file) which stores instrumental parameters, sample details. Therefore, imzml file can not be directly used. We also developed codes to generate Excel format pixel data from .imzml files of other vendor's proprietary MSI software are also amenable to the ratio imaging strategy described herein. Therefore, we include a R code for extracting pixel data directly from imzml file, regardless of source of datafile from different vendors. Notably, pixel-by-pixel metabolite imaging data can also be co-registered with other omics imaging datasets obtained from a sequential serial cryosection, independent of the need for a SCiLS lab license.

Given the lack of need for proprietary software to export pixel-by-pixel data, an individual feature list provides MALDI-MS instrument/application flexibility. Additionally, considering each pixel as a replicate from a defined ROI, exported pixel data can be readily used with either vendor-specific or non-proprietary metabolomics data software platforms for biomarker discovery and multivariate spatial metabolomics analysis such as principal component analysis (PCA), partial least-squares discriminant analysis (PLS-DA), hierarchical clustering (HCA), ROC curve assessment, VIP scoring, and pathway enrichment.[30-42]. Figure S1 shows an exemplary conversion of ROI pixel data to formats compatible with import into MetaboAnlayst[30] and Agilent Mass Hunter Professional. For the presented data, brain outer cortex regions were selected for comparison between mitochondrial cytochrome oxidase 10 (COXKO) and WT (n=4 for each genotype) mice.

**2. MSI ratio imaging requires missing pixel abundance annotation but not absolute metabolite concentration.** Missing value annotation is conventionally employed for interpretation of omics data, including metabolomics[43-46]. Spatial metabolomics data acquired from MALDI and DESI MSI studies are subjected to missing value annotation when features are undetected in a given pixel. Given the differences in cell types and ionization efficiency/suppression across tissue regions, missing values are more common in spatial MSI than LC/MS data from the same tissue, especially in the case of FT-ICR-MS, which uses a peak-picking threshold to filter out the bulk of signal noise generated from Fourier data transformation. To prevent potential inclusion of a missing value as "zero" abundance for imaging data analyses that include ROI metabolite mean abundance comparisons, we annotate missing values with 1/5 the minimum value quantified in all pixels in which it was detected. Figure S2 A-B show the indistinguishable images of exemplary metabolites before and after missing value annotation[30]. Therefore, pixel-wise missing value annotated data was used for all statistical analyses, image plots, and metabolite

194 ratio imaging described herein. To provide reciprocal and complementary images for easier ROI access
195 and visualization, we consider images for both A/B and B/A ratios (Figure S2 C-D).

196 It is possible that differences in ionization efficiency among metabolites may result in differential images
197 obtained from ion abundance ratio compared to concentration ratio. To test this, we quantify the absolute
198 concentration of brain glucose, lactate and ascorbate using stable isotope standards spiked into the
199 mimetic tissue sections prepared from carboxymethylcellulose (CMC) embedded brain homogenate.
200 Figure S3 shows similar ratio images among lactate, glucose and ascorbate obtained from abundance
201 data compared to quantified concentration data. While stable isotope standards and mimetic tissue model
202 are often used to obtain quantitative concentration of metabolite/lipid of interest, it is not applicable for
203 untargeted metabolite ratios that include an assessment of structurally undefined species. Note that the
204 utilization of our strategy is to provide untargeted (and targeted) ratio imaging as a hypothesis generation
205 tool and our quantification data indicate this use does not require absolute metabolite quantification.

206 **3. Pixel-by-pixel ratio imaging reduces cryosection preparation artefacts and improves data**
207 **interpretation**. Preparing cryosections from non-fixed and non-embedded tissues is a technically
208 demanding procedure prone to sectioning artefacts[47]. Tissue freezing, cryo-cut temperature variation,
209 section thickness irregularities and tissue storage can all affect imaging performance. Pixel-by-pixel
210 ratioing of metabolite/feature pairs offers the important advantage of reducing artefacts caused by non-
211 uniform matrix coating of cryosections and other elements of sample processing, especially for slides
212 containing multiple tissue cryosections. This is because as tissue cryosections are thaw-melted onto
213 slides individually, the layout sequence results in variable waiting times for completion of the mounting
214 process. Thus, individual cryosections undergo varying degrees of metabolically-active metabolite
215 degradation, even at the typical -20°C cryotome operating temperature.

216 Figure 2A-C and Figure S2B compare images for lysophosphatidylethanolamines (LPEs 18:1, 20:4, 22:4,
217 22:6) on brain sections from COX10 KO and WT mice. Lysophospholipids contain a free hydroxyl moiety
218 in either the sn-1 or sn-2 position of the glycerol backbone and are generated by phospholipase-mediated
219 (PLA1 and PLA2, respectively) hydrolysis of phospholipids. PLA1 hydrolyzes an ester bond at the sn-1
220 position, producing a saturated or monounsaturated fatty acid and a 1-lyso-2-acyl-phospholipid, while
221 PLA2 preferentially hydrolyzes unsaturated fatty acids at the sn2 position, producing polyunsaturated
222 fatty acids and a 2-lyso-1-acyl-phospholipid.

223 Notably, LPEs with polyunsaturated acyl chains of 20:4, 22:4 and 22:6 shown in Figure 2 predominantly
224 originate from PLA1 action. As shown, images of these individual LPEs are relatively diffuse and variable
225 among replicates of the same genotype (Figure 2 A-C). A relatively higher abundance of these species
226 was imaged in cross-sections of the striatal ventral region of the brain, except for LPE 22:6 in COX10 KO
227 brain, which was more abundant in the outer cortex. Note that 20:4 and 22:4 acyl chains are derived from
228 the ω6 fatty acids arachidonic acid (AA) and adrenic acid, while 22:6 acyl chains originate from an ω3
229 fatty acid, docosahexaenoic acid (DHA).

230 Ratio images of LPE 20:4 and LPE 22:4 to LPE 22:6 indicate higher relative abundance of ω6 to ω3
231 LPEs in the striatum ventral region compared to the outer cortex (Figure 2 D-F), consistent with the ratio
232 distribution of arachidonic acid to docosahexaenoic acid (Figure 2G). Compared to diffuse non-ratio
233 images of individual LPEs, the ratio images of ω6 to ω3 LPEs show an enhanced brain structure with
234 markedly sharper definition. Despite variable LPE values imaged between COX10 KO and WT brains,
235 overall LPE ratios were unchanged between genotypes. Note that we purposely chose this set of non-
236 ideal section quality and imaging data to demonstrate the clear benefit of ratio imaging in obviating
237 potential sample processing artefacts, thus improving image quality for data interpretation.

**4. Targeted metabolite ratio imaging may serve as a proxy for spatial enzyme and pathway activities among similar regions**. For a given enzyme, pixel-wise specific enzyme activity may be inferred from pixel-by-pixel ratio imaging of substrate-product metabolite pairs. However, due to differences in ionization efficiency, comparison of pathway activity can only be limited to the equivalent pixel/regions of tissues from different biological groups, given the assumption that ionization efficiency is identical for equivalent pixel from different tissue sections (i.e. same cell type and microenvironment), Notably, metabolites with similar functional structure in the same pathway are better fit for this application. For instance, fatty acids with different chain length, phospholipid with same head groups, nucleotide phosphates with different phosphorylation status are expected to have similar ionization efficiency in the same tissue pixel/region. Examples of metabolite ratios that may serve as readouts for comparative enzyme activities include glutamine to glutamate for glutaminase (GLS), aspartate to asparagine for asparagine synthase (ASNS), aspartate to N-acetylaspartate for N-acetyltransferase 8 (NAT8L), inosine monophosphate (IMP) to adenosine monophosphate (AMP) for AMP deaminase (AMPD), lactate to pyruvate for lactate dehydrogenase (LDH), N-acetyl-aspartyl-glutamate (NAAG) to N-acetyl-aspartate for NAAG synthetase (NAAGS), carnosine to histidine for carnosine synthase (CARNS), hexose to hexose phosphate for hexose kinase (HK), glutamate to oxyproline for 5-oxoprolinase (OPLAH), and glutathione disulfide to glutathione for glutathione peroxidase (GPX). Note that ratio image serves as a hypothesis generation tool, an orthogonal method may be needed for a higher degree of biological confidence.

For lipid related metabolites, ratios between different numbers of fatty acid double bonds for a given chain length (C16, C18, C20) would imply fatty acid desaturase (SCD) activity. Similarly, the fatty acid synthase (FAS) and PLA activities are reflected in the ratios of fatty acids with 2 carbon differences (C16 to C18, for example) and those of phospholipids to their corresponding lysophospholipids. Fatty acids are synthesized through metabolic pathways that include desaturation and elongation, sequentially producing a variety of long-chain saturated, monounsaturated, and polyunsaturated fatty acids (SFA, MUFA, and PUFA, respectively). Palmitic acid (FA 16:0) and stearic acid (FA 18:0) are the most common and abundant long chain saturated FAs in food and the human body. MUFAs synthesized from SFAs (via SCDs) are key components of phospholipids, triglycerides, and cholesterol esters that modulate cell membrane fluidity.

Obviously, pixel-by-pixel metabolite ratios are only possible for metabolite pairs detected and imaged within the same pixel of a given cryosection. MALDI-MSI using NEDC matrix and negative ion mode can detect all of the above-mentioned product-substrate pairs. Washing with acidic methanol significantly enhances the detection of phosphate-containing metabolites involved in energy metabolism[48]. Alternatively, using 9-Aminoacridine (9AA) as a matrix, purine and pyrimidine nucleotide mono-, di- and triphosphates can be imaged to obtain pixel-by-pixel ratios of nucleotides with different phosphate levels for assessment of relative phosphorylation status within a tissue.

Figure 3 demonstrates the benefit of imaging metabolically relevant metabolite ratio pairs in assessing regional gradients in enzymatic and metabolic pathways, as exemplified in E8.5 embryos at 10 μm (cellular) spatial resolution. Consistent with a role for the visceral yolk sac in providing nutrients, including glucose for embryo development, enhanced glycolytic activity was seen in the amnion and visceral yolk sac (Figure 3A-B). Furthermore, higher abundances of the desaturase product FA 18:1 relative to FA 18:0 (reflecting SCD activity) and of phophatidylethanolamine (PE) 38:4 relative to LPE 18:0 (reflecting PLA2 activity) are predominantly located in the allantois, head mesenchyme, and especially in the hindbrain neuroepithelium for FA 18:1 to FA 18:0 (Figure 3C, H). In contrast, the ratios of FA 16:0 relative to its elongation product FA 18:0, and DHA (ω3) relative to AA (ω6) fatty acids, showed opposite spatial distribution patterns (Figure 3D-E). Of note, similar ω3 to ω6 fatty acyl chain composition was also

observed for LPEs (Figure 3F-G). Interestingly, PLA1 and PLA2 appear to have quite different compartmented activities among yolk sac, amnion, and head mesenchyme (Figure 3G-H). These data offer promising and useful information for study of compartmented metabolism during embryo development at the single cell level, demonstrating the power of metabolite ratio imaging in spatial assessment of metabolic activity.

As an additional example, we present mouse hippocampus MSI findings, which show that ratio imaging may can provide additional cell-type specific metabolic information at cellular (10 μm) spatial resolution compared to individual metabolite imaging alone. For example, to assess the ATP phosphorylation status. Notably, neurons have higher energy requirements and prefer mitochondrial oxidative phosphorylation as their dominant energy source. In accord with this expectation, higher ATP/ADP, ADP/AMP, IDP/IMP ratios (Figure 3 J-L) are observed in neurons of mouse hippocampus, while indicators of oxidative stress (Figure 3I) and fatty acid synthesis (Figure 3P) were unchanged in neurons compared to other cell types. Elevated SCD and AMPD activities were also predominantly observed in neurons (Figure 3 M-N) compared to other cell types, consistent with SCD being a novel regulator of neuronal cell proliferation and differentiation and their reported immunocytochemical results[49]. Although a higher ratio of ω3 to ω6 fatty acids predicts improved hippocampus-dependent spatial memory and cognitive status in older adults[50], ratio imaging surprisingly shows that these neurons display a relatively lower level of DHA (ω3) to AA (ω6) fatty acids vs. other cell types in mouse hippocampus. Thus, ratio imaging findings have the potential to challenge existing concepts and guide further investigation.

Adipose tissues store body fat as neutral triglyceride and represent the chief energy reservoir in mammals. We previously reported that COX10 KO mice are typified by decreased white adipose stores, accelerated lipolysis with increased free fatty acid deposition and low leptin levels with decreased food intake[51]. We have since applied lipid and fatty acid ratio imaging to evaluate potential metabolic and enzymatic activities that may be responsible for the observed differences between COX10 KO and WT adipose tissue (Figure 4). As expected, distinct fatty acid and lipid profiles point to altered ω3 (DHA) to ω6 (AA) fatty acid composition (Figure 4A), fatty acid and lipid desaturation (Figure 4B-G), fatty acid synthesis (Figure 4H-J) and phospholipid hydrolysis (Figure 4K-L) in KO vs. WT adipose. Lower adipose ω3 to ω6 ratios have been associated with inflammation[52], obesity[53], altered gut microbiota[54,55] and other health problems[56,57]. These ratio imaging findings led us to speculate that the diminished ω3 to ω6 ratio in COX10 KO mice arises from an altered gut microbiome, supported by unpublished preliminary findings. This emergent hypothesis from ratio imaging analysis raises the clinically important possibility that supplementation of human COX10 mutant patients with ω3 fatty acids may effectively modify the microbiome to restore normalized adipose tissue composition and food intake. Note that ionization efficiencies and cryosection collecting method can impact the relative abundance of metabolites used in ratio computation and thereby the numeric ratio value itself. For example, the ATP/AMP ratio can change drastically from tissue collection, so can lysophospholipid to phospholipid ratio. Taken together, these results demonstrate the utility of ratio imaging as a valuable add-on MSI approach to probe for potential regiospecific changes in cellular metabolic activities.

**5. Metabolite ratios uncover genotype-specific and spatially resolved tissue regions**. Conventional MSI depicts relative spatial abundance of metabolite features in tissue regions. For defined structures in tissues such as brain, kidney and prostate, metabolite images can potentially recognize discrete tissue structures, under the condition that ionization efficiency and/or absolute abundance differences do indeed exist among these structurally defined loci. In contrast, pixel-by-pixel metabolite ratio imaging almost invariably resolves distinct tissue structures but also uncovers fine structure and anatomically unrecognized regions not revealed by individual metabolite imaging alone.

Using COX10 KO and WT mouse coronal brain sections as an example, we observed that individual glutamate, aspartate and glutamine distribution images failed to show a clear structural distribution, (Figure 5A-C). However, ratio imaging revealed a 1.59-fold increase in aspartate to glutamate ratio in an unusual "moon arc" region across the amygdala and hypothalamus (mean abundance 0.563 in 6345 pixels) relative to the rest of the coronal brain (mean abundance 0.353 in 45742 pixels, Figure 5D). Similar but different arc-like structures are encompassed within the ventral thalamus and hypothalamus, wherein glutamate to glutamine ratio show a 1.63-fold increase in intensity compared to the rest of the brain (mean abundance of 0.695 in 7108 pixels vs 0.428 in 44979 pixels, Figure 5E), while relative glutamine to aspartate abundance appears enriched in the striatum (Figure 5F). Thus, ratio imaging not only improves image quality for regional/cell-selective assessment of metabolite distributions but also offers an opportunity to discover new differentially metabolic regions with biological relevance. Note that the enrichment of aspartate to glutamate and glutamine to glutamate near the thalamus, nucleus accumbens (NAc) and hypothalamus (and visualization of their reciprocal ratio images) were robust and consistently reproduced in MALDI-MSI experiments using an independent cohort of COX10 KO and WT mouse brains (Figure 5G-H). Enrichment of glutamate to aspartate in the cortex region was further confirmed in horizontal and sagittal brain sections from random mouse brains (Figure 5I-J).

Considering the above, it is notable that aberrations in glutamate, glutamine and aspartate homeostasis are all implicated in neurological disease[58,59]. Aspartate serves as an amino donor for glial glutamate formation[60], and the hippocampal aspartate to glutamate ratio has been related to changes in brain glucose[61]. Glutamine is synthesized from glutamate and ammonia by the catalytic action of glutamine synthetase (GS) in glial cells of the brain, while it is also taken into neurons and generates glutamate and ammonia by the catalytic action of glutaminase. The glutamate-glutamine cycle is closely linked to cellular energy metabolism[59], and ratios between neurotransmitters (GABA, glutamine and glutamate) have been used in MRS studies to probe neurological disease mechanisms and progression[62,63]. Specifically, ratios among glutamine, glutamate and aspartate have been implicated in memory function[64], schizophrenia, depression, alcoholism and motivated performance via NAc[65]. Given the biological significance of these ratios, spatial ratio imaging can reveal previously unrecognized ROI and relative abundance ratio differences between disease and normal physiological states. In COX10 KO and WT brains, differential aspartate to glutamate and glutamine to glutamate ratios point to an interesting linkage between muscle health and brain neurotransmitter signaling: mitochondrial myopathy alters glutamine, glutamate and aspartate signaling near the NAc. This unusual finding is in accord with and supportive of our recent discovery of a coordinated multiorgan metabolic response that extends to the brain and is anticipated to play a role in human mitochondrial myopathy disease states[51].

**6. Spatial correlation of ratio and non-ratio pixel-by-pixel data as an additional discovery tool**. Combining pixel-by-pixel ratio and non-ratio data offers an additional tool for spatial metabolism discovery. Despite that MALDI MSI is a soft ionization technique, it generates various adduct ion clusters and possible fragment ions from common neutral losses. Unknown non-ratio metabolite feature data in a given ROI can be combined with known metabolite ratios, pixel-by-pixel, to discover correlations between unknowns and metabolite ratios that inform on a specific enzyme activity or metabolic pathway. This application can reveal unrecognized but significantly correlated pathway metabolites and metabolite ratios, thus enabling recognition of unknown metabolites with relevance to specific pathways of interest.

Using COX10 KO and WT mouse adipose as an example, the unknown [M-H] 375.23059 was negatively correlated with the ratios of PA 36:4 to LPA 16:0 and PA 36:1 to PA 18:1, indicating that the abundance

of this unknown metabolite may be positively associated with PLA1 and/or PLA2 activity (Table 1). Given that PLA1 and PLA2 generate different products, with PLA1 dominantly yielding unsaturated lysophospholipids and PLA2 yielding saturated lysophospholipids, an observed negative correlation of the unknown with LPA 18:1 to LPA 18:0 ratios hints that it may originate as a product of PLA2. Indeed, direct correlation of this unknown with lipid metabolites suggests it could be a reduction product of CPA 16:0 after loss of one oxygen atom, matching the formula $C_{19}H_{37}O_5P$ with 0.013 ppm mass accuracy. While it remains to be established that this unknown is a *bona fide* reduction product of CPA 16:0, the example illustrates how pixel-by-pixel correlations of unknown metabolite masses with metabolite ratios can aid potential discovery of pathway-relevant metabolites.

Another example of correlation-based discovery comes from consideration of COX10 KO and WT mouse brain sections, where calculating the Spearman correlation of combined pixel data from both individual metabolites and metabolite ratios revealed an unexpected positive association of $FeCl_2$ with the glutamate to glutamine ratio, along with other related metabolite ratios that include aspartate, NAA, glucose and glutathione (Table 2, Figure S4). Conversely, glutamine to glutamate ratios showed significant negative correlation with $FeCl_2$ and the above-mentioned metabolites (Table S2), suggesting these correlations are neither random nor an artefact of missing value annotation. Notably, free iron is recognized as a key mediator of glutamate excitotoxicity in spinal cord motor neurons[66]. Significant associations between peripheral markers of iron metabolism and glutamate with glutamine in relation to total creatine (Glx:tCr) concentration has been reported in female human brains[67]. Glutamate facilitates divalent metal transporter 1 (DMT1) flux and subsequent increases in brain free iron content[68]. A positive relation between iron and glutamate in the brain and other organs has also been reported[60,61,66,67,69,70].

Note that this correlation with $FeCl_2$ was observed in all brain sections regardless of genotype. Ferrous iron, measured as its chloride adduct when detected with NEDC matrix, likely arises from both free labile iron and protein-bound iron. Decreased $FeCl_2$ levels in combination with decreased glutamate in the cortex region of COX10 KO vs. WT brain is an unexpected but intriguing finding. While aging is associated with increased brain iron through cortex-derived expression of the iron regulatory hormone hepcidin[71], calorie restriction down-regulates hepcidin expression[72]. In accord with decreased $Fe^{2+}$ and glutamate to glutamine ratio, COX10 KO mice exhibited decreased food intake and adopted a metabolic state resembling caloric restriction[51]. Collectively, pan-correlation of targeted metabolite ratios with non-ratio data serve as an additional imaging tool for data interpretation and hypothesis generation.

**7. Metabolite ratios for PCA tissue segmentation in complex tissue sections.** Spatial segmentation is a popular application in MSI to cluster regions with similar metabolite abundance profiles. Unsupervised MSI segmentation methods such as PCA, K-means, bisecting K-means and HCA are all often used to delineate underlying tissue structures from high-dimensional MSI data without prior knowledge of sample anatomical information. Most segmentation approaches rely on unsupervised clustering algorithms that can readily result in the generation of biologically unrealistic tissue structures. Various algorithms for integrating partial or prior structural information with unsupervised clustering have been reported to improve segmentation results[73-79].

To date, tissue segmentation utilizing pixel-by-pixel metabolite ratio data for imaging differential metabolic zones has not been reported. We hypothesized that metabolite/feature ratios may generate more meaningful biologically relevant ROIs due in part to reduction of systematic experimental noise. Mouse brain sections serve as a good example for the utility of this approach. As expected, consideration of 10 different glutamate/glutamine related metabolites for PCA analysis (Table S3) with ratios involving the

422 top 5 components generated an interesting arc-shaped region that encompasses the hypothalamus,
423 striatum and NAc, while non-ratio metabolite data did not (Figure 6A). This metabolite ratio PCA result
424 was used to provide an RGB image capturing the structure of the dataset by mapping the first of the five
425 principal components. Apparently, this segmentation result captures and maintains the enriched arc-like
426 regions shown previously in neurotransmitter ratio images (Figure 5D-E and G). Since glutamate plays
427 key roles linking carbohydrate and amino acid metabolism via the tricarboxylic acid (TCA) cycle, as well
428 as in nitrogen trafficking and ammonia homeostasis in the brain, this region likely exhibits unique
429 glutamate-related metabolism and warrants further investigation. Likewise, a more defined outline of
430 striatum and cerebellum in the coronal brain structure was obtained in PCA segmentation using the top
431 5 component metabolite ratios as well as 5 LPEs (Table S4) but was not observed with these 5 LPEs
432 alone (Figure 6B).
433
434 As metabolite ratio data can segment tissue into novel ROIs, we considered the possibility that differential
435 metabolite ratios can serve as markers to distinguish genotypes, either independently or when combined
436 with individual metabolites. In COX10 KO and WT mouse brains, ratios among three neurotransmitter-
437 related non-glutamate metabolites (glutamine, aspartate and homocarnosine) show clear differences
438 within the cerebral cortex for glutamine to aspartate ratios (Figure 7A) and within the ventral striatum for
439 homocarnosine to glutamine and homocarnosine to aspartate ratios (Figure 7 B-C).
440
441 The interrelationship of glutamine, aspartate and homocarnosine is shown in Figure 7D. Homocarnosine
442 is a naturally occurring imidazole-containing dipeptide uniquely present in the brain, likely in a subclass
443 of GABAergic neurons[80]. It is synthetized from γ-aminobutyric acid (GABA) and histidine via
444 homocarnosine synthase (CARNS1) and can be hydrolyzed to histidine and GABA by carnosine
445 dipeptidase 1 (CNDP1), which is exclusively expressed in brain (Figure 7D). Homocarnosine is
446 recognized to play a role in mediating neuronal activity during satiation and starvation[81]. It is decreased
447 in the brain during cold adaptation[82] and increased during alcohol intoxication[83]. Additionally, aspartate
448 and glutamate can be exchanged across the inner mitochondrial membrane by mitochondrial carrier
449 protein SLC25A12 (Aralar1), mainly distributed in brain and skeletal muscle for the transport of aspartate
450 from mitochondria to cytosol, and in the transfer of cytosolic reducing equivalents into mitochondria as a
451 member of the malate-aspartate shuttle[84]. Given the interrelationship of these three metabolites and their
452 important roles in maintaining brain neurotransmitter pools, their ratios could report on neurotransmitter
453 homeostasis. Indeed, it has been shown that brain function can be estimated from the ratio of glutamine
454 to homocarnosine in cerebrospinal fluid[85]. An early report showed that homocarnosine is elevated in
455 monkey brain in the setting of a protein-deficient diet, whereas aspartate and glutamate levels are
456 unchanged[86]. Similarly, in COX10 KO and WT brains, we observed no difference in individual aspartate
457 or glutamate levels (Figure 5 A-B), while striatal homocarnosine (Figure 7E) and glutamine (Figure 5C)
458 were elevated. As COX10 KO mice displayed altered food intake, muscle mass and elevated starvation
459 response[51], an elevated homocarnosine to glutamine and glutamine to glutamate ratio (Figure 5F) could
460 indicate increased synthesis of homocarnosine via the glutamine-glutamate-GABA axis. These results
461 indicate that ratios among the three metabolites could serve as alternative markers to distinguish these
462 murine genotypes.
463
464 To provide additional spatial detail, we performed PCA segmentation on COX10 KO and WT brains using
465 ratio and non-ratio pixel data for homocarnosine, glutamine and aspartate with the goal of learning
466 whether differential ROIs exist for these genotypes. In this PCA segmentation, the overview RGB image
467 maps the first three principal components to the red, green and blue channels respectively. Comparing
468 PCA overview images from ratio (Figure 7F) to non-ratio (Figure 7G), PCA results from ratios showed

469 cyan blue located in larger areas of striatum and thalamus regions in KO relative to WT brains, while non-
470 ratio PCA did not. These results reveal distinguishable differences in abundance in the cyan region of
471 the KO and WT brain regarding interconversion and homeostasis of the three neurotransmitter-relevant
472 metabolites. Therefore, metabolite ratios could serve as better candidates for ROI-based disease
473 metabotyping.
474
475 **8. UMAP using metabolite ratios enables spatial metabotype mapping and recognizes novel ROIs**.
476 Unlike PCA analysis, which builds on a linear dimension reduction algorithm, uniform manifold
477 approximation and projection (UMAP) is a relatively newer non-linear dimension reduction algorithm often
478 used to visualize complex dataset while preserving local structure. UMAP projects dimensionally reduced
479 data into 2D or 3D scatterplots. Samples close to each other in the scatterplot have similar fingerprints,
480 while samples further away have progressively different profiles. It is often used in combination with other
481 clustering algorithms such as HCA and K-mean clustering to identify subgroups in the projected space.
482 UMAP has been widely used for omics data interpretation to find internal structure in mixed datasets, as
483 well as for disease subtyping, single cell bioogy[87-89] and various molecular imaging applications.
484
485 Since metabolite ratio segmentation using PCA is less prone to section preparation artefacts in MALDI-
486 MSI and enables genotype-specific tissue segmentation (Figure 7F), we sought to assess whether
487 metabolite ratio UMAP and clustering could generate novel ROIs that enable new spatial metabotype
488 mapping beyond that obtained from consideration of individual metabolites. UMAP analysis of ratios for
489 5 LPEs in COX10 KO and WT murine brain sections, followed by K-mean clustering, showed much more
490 defined and biologically relevant ROIs than those derived from non-ratioed LPEs (Figure 8) that resemble
491 PCA segmentation results (Figure 6B). This UMAP analysis used 9 neighbors with 2 Euclidean
492 components as metric measurements of similarity. Figures S4-5 show the nine segmented ROIs from
493 ratio and non-ratio UMAP and K-mean clustering analyses, along with scatterplots of the first 2 UMAP
494 components (V1 vs. V2), projecting the distribution and similarity of each of 9 segmented ROIs. While
495 non-ratio segmented ROIs did not provide comparable and confident ROIs among replicates (Figure S5),
496 the ratio-segmented data indicate a distinct LPE profile between the outer cortex (ROI 3), cortex (ROI 8),
497 ventral thalamus (ROI 5) and striatal regions (ROI 2) (Figure S6). These ROIs generated by UMAP
498 metabolite ratios enable visualization and a reproducible comparison of lipid metabolite and/or ratio
499 abundance among these irregular and difficult-to-draw (i.e. with imprecise anatomical definition) regions.
500 In addition, they provide unique ROIs for pixel-by-pixel metabolite correlation with other previously
501 mentioned multivariate analyses (Table 1, Figure S1)
502
503 Differences in metabolite abundance among ROIs can be difficult to visualize if the image color scale is
504 set too wide. ROI images are better visualized by applying a relative image abundance scale set to a
505 discrete ROI, rather than the entire tissue section. UMAP segmentation using ratios provides novel ROIs
506 for such purpose. For example, murine brain imaging results showed decreased aspartate to NAA ratios
507 visualizable in almost all 8 ROIs investigated with COX10 KO relative to WT, suggesting overall
508 diminished expression or activity of NAT8L, the neuronal enzyme that produces NAA from acetyl-CoA
509 and aspartate (Figure S7 A-H). Moreover, NAAG, the most abundant dipeptide in the brain, can be
510 synthesized from NAA and glutamate by NAAG synthase. NAAG to NAA and aspartate ratios were
511 greater in ROI 7 of KO compared to WT brain (Figure S7 I-J), suggesting elevated NAAG synthase activity
512 in this defined region. Of note, NAT8L mRNA oxidation is linked to neurodegeneration in multiple
513 sclerosis[90] and overexpression-induced vulnerability to depressive behavior in mice[91]. NAAG functions
514 as a retrograde neurotransmitter and is released in response to glutamate, providing postsynaptic
515 neurons with a feedback mechanism to inhibit excessive glutamate signaling[92]. Therefore, elevated

516 NAT8L activity, indicated by an increased NAA to aspartate ratio, is consistent with observations that
517 COX10 KO mice are less mobile and relatively inactive compared to WT. Reviewing the non-ratio images
518 of these metabolites, NAAG is mainly enriched near ROI 7 visualized in whole section images (Figure S8
519 A), consistent with higher abundance of NAAG, NAA and glutamine imaged exclusively in COX10 KO
520 ROI 7 (Figure S8 B-D). These changes contrast with the decreased aspartate and unchanged glutamate
521 levels imaged in ROI 7 of KO brains (Figure S8 E-F). Therefore, we infer that the COX10 KO brain exhibits
522 increased NAA and NAAG syntheses as feedback to inhibit excessive glutamate signaling. In contrast,
523 glutamate within the NAc showed no change compared to WT, potentially due to excess glutamate being
524 used for synthesis of glutamine and NAAG, which are elevated in KO ROI 7 (Figure S8 C-D).
525 Consideration of these UMAP findings exemplifies the applicability of this strategy for MSI data
526 interpretation.
527
528 UMAP derived ROIs can be applied to survey metabolite abundances, pixel-by-pixel, for correlation
529 analysis in ROIs from a large combined dataset that includes metabolite ratio and non-ratio pixel data,
530 as shown previously for whole tissue sections (Tables 1 and 2A). When correlation is narrowed to a
531 specific ROI and genotype, regional correlation results can be very different from global correlations.
532 Figure S8 show pixel-by-pixel correlation of the glutamine to glutamate ratio, along with a compendium
533 of all detected metabolites and ratios contained in a UMAP-generated ROI 7, comparing COX10 KO and
534 WT brain. For improved correlation plot visualization, only significant correlations with Spearman
535 correlation coefficients >0.4 are presented in Figure S9. Glutamate to glutamine ratio positively
536 correlated with glutamate, while negative correlations were observed for NAAG and NAAG/NAA in both
537 WT and KO ROI 7 (Table S5). These findings are consistent with existing knowledge that NAAG synthesis
538 inhibits excess glutamate signaling.
539
540 Given that LPE ratios can be used as a tool for brain segmentation and to overcome variations in section
541 quality, we asked if UMAP with the same 5 LPE ratios can similarly be applied for other types of brain
542 section ROI segmentation. As predicted, UMAP generated ROIs consistent with brain anatomy in two
543 separate experiments depicted by horizonal and sagittal brain sections (Figure S10). Collectively, UMAP
544 analyses using metabolite ratio imaging provide a novel and robust tool to spatially-map tissue
545 microenvironments, revealing matched localized differences among test groups.
546

547 **Discussion**

548 Analyses that utilize metabolite ratios are not a new concept in omics investigations, particularly for
549 applications that involve medical MRI spectroscopy-generated imaging data. Notwithstanding, an
550 unbiased strategy and application of pixel-by-pixel imaging of targeted and untargeted metabolite ratios
551 for MSI data interpretation has been lacking. We demonstrate that ratio imaging adds a powerful new
552 tool to mitigate sample preparation artefacts, to spatially metabotype tissue microenvironments, and to
553 reveal spatially distinct functional variations in enzymatic and metabolic pathway activities.

554 Metabolite ratio imaging can uncover previously unrecognized biology, as exemplified here for the pixel-
555 by-pixel distribution and metabolic interplay among neurotransmitter-related brain metabolites.
556 Glutamate, glutamine, aspartate, histidine, homocarnosine and GABA are all well-recognized brain
557 metabolites that contribute to fundamental brain activities, including synaptic transmission and energy
558 production. Their ratios are tightly regulated for maintaining proper brain function and vary across
559 different regions of the brain and under different physiological conditions. Disturbance of these ratios can
560 be deleterious to neurotransmission and overall brain health. Imaging of ratios among these and all other

561 metabolites engenders a novel mapping tool that may point to localized segmentation of metabolic
562 activities not recognized by imaging individual metabolites. Considering ratios as proxies of enzyme
563 reaction rates between substrate and product, ratio-derived ROIs along with their ratio and non-ratio
564 abundances offer a novel strategy for study of disease pathophysiology, biomarker discovery and
565 identification of new therapeutic targets (Figures 5-7).

566 As described, untargeted pixel-by pixel ratios can be derived from all detected mass spectral features,
567 irrespective of whether the features have known structural identities. Combined with non-ratio feature
568 data, information-rich metabolite ratio datasets offer great potential for association with other imaging or
569 spatial omics data. Notably, generation of metabolite ratio datasets can be performed using the described
570 R-code algorithm and applied pixel-by-pixel to individual metabolite features that have been incorporated
571 into an ExcelL.csv format file with spot ID and pixel axis positional information. Furthermore, R codes for
572 generating pixel data directly from .imzml files provide a convenient way to perform spatial ratio analysis
573 for all types of MSI experiments. For pixel data with ≤10 μm raster width, single cell spatial imaging and
574 omics data can ideally be associated with untargeted metabolite/feature ratio data to achieve single cell
575 multiomics metadata integration. For this purpose, a P-gain can be applied to filter out significantly
576 correlated associations, as previously described for some well-established GWAS and MWAS
577 association studies[24-27]. A potential challenge for single cell metabolomics spatial data interpretation lies
578 in possible concerns regarding metabolite data co-registration with anatomical or other single cell omics
579 datasets. Notably, when datasets are obtained from serial sections, a mere 10 μm shift could result in
580 cell layer disparities.

581 Combining ratio and non-ratio pixel data offers a powerful new tool to survey significant but unappreciated
582 global correlations between metabolites ratios (both structurally defined and undefined) in distinct ROIs
583 that are revealed by metabolite ratio tissue segmentation. Among other unexpected findings, we
584 demonstrate that an elevated glutamine to glutamate ratio is observed in COX10 KO brain compared to
585 WT within the NAc and that this ratio positively correlates with ferrous iron levels and Nat8L enzymatic
586 activity (inferred from NAA to aspartate ratios, Table 2, Figures S3 and S8). These associations were
587 previously unrecognized but are consistent with a whole-body feed-forward action of mitochondrial
588 myopathy on levels of brain leptin, corticosteroids and neurotransmitter signaling[51].

589 Applying targeted and untargeted metabolite ratios for PCA and UMAP tissue segmentation generates
590 novel and artefact-free ROIs linking proxy metabolic activity. One limitation for MSI ratio data
591 interpretation is that the coverage of known metabolite structures and pathways is considerably less
592 (typically 200-300 structurally identified species) than for LC/MS analyses. It is important to note that
593 combined ratio and non-ratio data can also be used for segmentation. However, segmentation results
594 using combined ratio and non-ratio data may be confounded by artefact-prone non-ratio metabolite data
595 and thus not as clean as those using ratio alone. We speculate that combining metabolite ratios from
596 different metabolic pathways may segment tissue with ROIs more representative of real metabotypes.

597 In summary, we anticipate targeted and untargeted metabolite ratio imaging to provide a powerful add-
598 on tool for MSI experiments, revealing otherwise hidden information in acquired datasets. These ratios
599 may serve as potential new biomarkers to distinguish anatomically distinct metabolic tissue regions and
600 uncover otherwise unrecognized differences in either physiological cell function or from differing cellular
601 responses to drug treatments and disease states. This ratio imaging strategy can be further extended to
602 image pixel-by-pixel fractional abundance of isotopologues for targeted and untargeted MALDI-MSI
603 stable isotope tracing. When coupled with the FT-ICR high resolution mass spectrometer, simultaneous
604 imaging of isotopologue incorporation is possible for tracing molecules containing mixed stable isotope
605 elements (e.g. $^{13}C$, $^{15}N$, $^{2}H$, $^{18}O$, $^{34}S$).

## Acknowledgements

We are thankful for Drs. Tal Nuriel, Eileen Ruth Torres, Li Gan for sharing mouse brain images used in this paper. NIH support by 1S10OD023652 (SG) for WCM's Ultra-high Resolution MALDI-FT-ICR Imaging Core Facility. NIH 5 R01 AR076029-03A1 (QC and MD), R21 NS118233-01A1 (QC and MD), R21 ES032347(QC).

## Author contributions

HC, DM, NS, PP, JF, IT, JMS, CK, CY and FH; MALDI MS sample preparation and data analyses. HC, SSG, KRK, MD and QC; conceptualization, HC and QC; writing.

## Conflicts of Interest

Joshua L. Fischer is a Bruker employee.

621 **Figure legends**
622
623 **Figure 1.** Schematic workflow of metabolite ratio imaging using pixel data from Bruker SCiLS Lab API
624 or imzml file from any MSI data source. For SCiLS lab MSI data, the execution of R codes starts with
625 connecting a local SCiLS lab session project in R studio. Installation of SCiLS lab is required for this
626 connection. After pixel data for a feature list is generated and exported as an Excel csv file, SCiLS lab
627 installation is not required for downstream ratio imaging and data analysis, except for the potential writing
628 of a spot image with labels back to SCiLS lab. For other types of MSI data, R code execution extracts
629 pixel data from imzml file for subsequent ratio imaging and analysis.
630
631 **Figure 2.** Pixel-by-pixel ratio image visualization reduces cryosection preparation artefacts and enables
632 spatial metabolic discovery in COX 10 KO mouse brain (left 4 sections) compared to WT (right four
633 sections). Panel A-C: blurry and diffused images of LPEs with ω3 (A-B) and ω6 (C) polyunsaturated fatty
634 acyl chains; Panel D-F: sharper ratio images of ω3 fatty acid containing LPE 20:4 and LPE 22:4 to ω6
635 fatty acid containing LPE 22:6; Panel G: ratio image of ω6 arachidonic acid (FA 20:4) to ω3
636 docosahexaenoic acid (FA 22:6) is consistent with the identified abundance ratio distributions for LPE
637 20:4 and LPE 22:4 to LPE 22:6.

638 **Figure 3.** Metabolically relevant metabolite ratio pairs that probe enzymatic and metabolic pathway
639 activity in E8.5 mouse embryo cryosections and mouse hippocampus at 10 μm spatial resolution. Panel
640 A: representative structure of E 8.5 embryo from an H&E stained embryo serial section. Panel B-H: Ratio
641 of substrate/ product pairs of glycolysis, fatty acid and lipid metabolism that imply compartmented
642 activities for hexokinase (B), fatty acid desaturation (C), fatty acid chain elongation (D), fatty acid
643 composition (E-F) and phospholipase activity (G-H) in E 8.5 embryos. Panel I-Q: Ratio images showing
644 relative oxidative stress (I), adenine nucleotide energy levels (J-L), purine nucleotide cycle activity (M-N),
645 fatty acid desaturation(O), synthesis (P), ω3:ω6 FA ratio (Q) in neurons (purple arrow), compared to
646 other cells in mouse hippocampus.
647
648 **Figure 4.** Altered fatty acid and lipid metabolism probed by ratio imaging in adipose tissue from COX 10
649 KO vs. WT mice. COX 10 KO, left 4 sections; WT, right 3 sections. Imaging data was acquired at 80 μm
650 spatial resolution. Panel A: Decreased abundance ratio of FA 22:6 (DHA, ω3 fatty acid) to FA 20:4 (AA,
651 ω6 fatty acid) in COX 10 KO adipose tissue. Panel B-C: Decreased fatty acid FA 16:0 and FA 18:0
652 desaturation in COX 10 KO adipose. Panel D-E: Decreased desaturated fatty acid abundance ratios for
653 lysophospolipids and phospholipids in COX 10 KO adipose tissue. Panel H-J: Elevated fatty acid
654 synthesis inferred by free fatty acid and phospholipids ratios, considering FA 18:0 to FA 16:0 (H-I) and
655 FA 20:1 to 18:1 (L) in COX 10 KO adipose. Panel K-L: Elevated PLA2 (K) and PLA1(L) activities implied
656 by the elevated ratio of Lyso PA to PA in COX 10 KO adipose.

657 **Figure 5.** Ratio imaging uncovers novel mouse brain regions with genotype-specific and spatially
658 resolved ratios of aspartate, glutamate and glutamine. Panel A-C: images of glutamine, glutamate and
659 aspartate in coronal sections of COX 10 KO (left 4 sections) and WT (right 4 sections) mouse brains.
660 Panel D-F: Differential abundance ratios of aspartate, glutamate and glutamine observed in defined
661 regions of the COX 10 KO and WT brains. Panel G-H: Reciprocal and differential aspartate to glutamate
662 ratio and Arc-like NAC containing region was repeated in a separate group of COX 10 KO (left 4 sections)
663 and WT (right four sections) mouse brains. Panel I-J: Enrichment in the glutamate to aspartate ratio in
664 the cortex region of mouse brain, as revealed in horizonal and sagittal sections.
665

666 **Figure 6.** PCA segmentation of mouse brains comparing ratio and non-ratio metabolite pixel data. Panel
667 A: PCA considering the top 5 components from ratios of 10-glutamate related metabolites that reveal an
668 unanticipated arc-like regional distribution within the hypothalamus, striatum and NAc, that is not detected
669 by consideration of only non-ratio metabolite data. Panel B: PCA considering the top 5 components of 5-
670 LPE metabolites showing fine brain structure that is not fully represented by only non-ratio metabolite
671 segmentation.

672 **Figure 7.** Metabolite ratios for segmentation and biomarker discovery in segmented ROIs. KO: right 4
673 sections; WT: left 4 sections. Panel A-C: Ratio images of homocarnosine, glutamine and aspartate.
674 Panel D: Enzymatic regulation and interconversions among brain glutamine, aspartate and
675 homocarnosine. Panel E: Image of homocarnosine. Panel F: PCA with top 5 components and using ratios
676 of homocarnosine, glutamine and aspartate shows differential ROI abundance shown in cyan blue in
677 larger area of striatum, thalamus hypothalamus regions in KO compared to WT. Panel G: PCA with top
678 5 components using homocarnosine, glutamine and aspartate pixel data show indistinguishable ROIs
679 between genotypes.

680 **Figure 8.** UMAP analysis using 5 LPEs ratio followed by K-mean clustering on COX KO and WT brain
681 sections shows a much cleaner and biologically relevant ROIs compared to those of LPE non-ratio. Panel
682 A: UMAP clustering using ratios of 5 LPEs. Panel B: UMAP clustering using 5 LPE pixel data. The list of
683 5 LPEs is shown Table S4. Nine neighbors, 2 components with Euclidean distance as metric
684 measurement of similarities were used in this UMAP analysis.

685 **Figure 9.** Ratio of glutamate to glutamine and $Fe^{2+}$ abundance are co-enriched in the outer cortex of
686 the COX10 KO (right 4 sections) and WT (left 4 sections) brain.

687

688 **Supplemental figures**

689 **Figure S1** Application of pixel-by-pixel exemplary MALDI MS imaging data to metabolomics multivariate
690 analysis using free or commercially available software package. Panel A: ROIs of COX 10 KO (left 4
691 sections) and WT (right 4 sections) brain outer cortex; Panel B: PLS-DA score plot showing classification
692 of COX 10 KO and WT cortex pixels using Metaboanalyst 5.0
693 (https://www.metaboanalyst.ca/MetaboAnalyst/ModuleView.xhtml). Panel C: Variable importance in
694 projection (VIP) scores of metabolites from PLS-DA shown in panel B. The colored boxes on the right
695 indicate the relative concentrations of the corresponding metabolite in COX 10 KO and WT. Panel D:
696 Matched pathways showing p values from the pathway enrichment analysis and pathway impact values
697 from the pathway topology analysis. Differential metabolites imaged in cortex of COX 10 KO vs WT brain
698 and metabolite quarries from KEGG mouse metabolic pathway were used in this analysis. Panel E:
699 Metabolite set enrichment analysis showing enrichment ratio of metabolic pathway metabolites.
700 Differential metabolites from cortex of COX 10 KO vs WT and the Small Molecule Pathway Database
701 (SMPDB) were used for this analysis. The enrichment analysis resembles gene set enrichment analysis
702 in transcriptomics. Panel F: Metabolite correlation heatmap generated from differential metabolites in
703 cortex of COX 10 KO and WT. Metaboanalyst 5.0 was used for analyses shown in panel B-E and Agilent
704 MassProfiler Professional 15.1 was used for analysis in shown in panel F.

705 **Figure S2** Exemplary MALDI MSI images generated before (A) and after (B) missing value annotation
706 and from reciprocal ratios (C-D). MSI Data was acquired at 80 µm using NEDC as matrix.

707 **Figure S3** Ratio images obtained from metabolite ion abundance exhibit similar characteristics to those
708 generated from absolute metabolite concentration. Panel A-C: Images of mouse brain and mimetic brain
709 sections spiked with stable isotope labeled [1-$^{13}$C] lactate (A), [U-$^{13}C_6$]glucose (B) and [1-$^{13}$C]ascorbate
710 (C). The concentrations of stable isotope standards from middle to left column of the slide are: 0, 1, 2.5,
711 5.0, 7.5, 10.0, 12.5, 15.0 mM for [1-$^{13}$C] lactate; 0, 2.5, 0.5, 1.0, 2.5, 5.0, 7.5, 10mM for [U-$^{13}C_6$]glucose ;
712 and 0, 0.05, 0.10, 0.25, 0.50, 0.75, 1.0, 1.5 mM for [1-$^{13}$C]ascorbate. Panel D-F: Calibration curves for
713 [1-$^{13}$C] lactate (D), [U-$^{13}C_6$]glucose (E) and [1-$^{13}$C]ascorbate (F). Panel G-L: Ratio images from
714 abundance ratio (upper image) verse concentration ratio (lower image).

715 **Figure S4** Ratio of glutamate to glutamine and $Fe^{2+}$ abundance are co-enriched in the outer cortex of
716 the COX10 KO (right 4 sections) and WT (left 4 sections) brain.

717 **Figure S5** ROIs and UMAP scatter plots generated from non-ratio metabolite data. Panel A-I: Nine
718 segmented ROIs generated UMAP and K-mean clustering analysis corresponding to clustered regions
719 of 1-9. Panel J: Scatterplot of UMAP first 2 components (V1 vs V2) projecting the distribution and
720 similarity of 9 segmented ROIs resulting in a incomplete and inconsistent ROIs among replicates. 5 LPE
721 (Table S3) pixel data was used for UMAP analysis.

722 **Figure S6** ROIs and UMAP scatter plots generated from metabolite ratio data. Panel A-I: Nine
723 segmented ROIs generated UMAP and K-mean clustering analysis corresponding to clustered regions
724 of 1-9. Panel J: Scatterplot of UMAP first 2 components (V1 vs V2) projecting the distribution and
725 similarity of 9 segmented ROIs shows a distinct LPE profile between outer cortex (ROI 3) cortex (ROI 8)
726 and ventral thalamus (ROI 5) striatum region(ROI2). Ratio of 5 LPE (Table S3) pixel data was used for
727 UMAP.

728 **Figure S7** Ratio images of NAA, NAAG and aspartate for UMAP-generated ROIs. Panel A-H: Ratio
729 image of NAA to aspartate in 8 UMAP-segmented ROIs. Panel I-J: Ratio images of NAAG to NAA (I)

730 and NAAG to aspartate in ROI 7 of UAMP segmented ROIs. COX10 KO, right 4 sections; WT, left 4
731 sections.

732 **Figure S8** Images of NAAG and neurotransmitter related metabolites visualized in UMAP-generated
733 ROI 7. Panel A: NAAG is enriched and elevated in in ROI 7–like region of COX 10 KO brain. Panel B-D:
734 NAA,NAAG and glutamine are elevated in ROI 7 of COX 10 KO brain. Panel E: decreased level of
735 aspartate in ROI 7 of COX10 KO; Panel F: Glutamate shows no change in ROI 7 of COX 10 KO compared
736 to WT. COX10 KO, right 4 sections; WT, left 4 sections.

737 **Figure S9** Pixel-by-pixel correlation of glutamine to glutamate ratio with a compendium of all detected
738 metabolites and ratios exclusively in UMAP-generated ROI 7, comparing WT (A) to COX 10 KO (B) brain.
739 4 biological replicates for each genotype. Only significant correlations with a spearman correlation
740 coefficient of greater than 0.4 were presented in the figure.

741 **Figure S10** UMAP using 5LPE ratios generated ROIs consistent with brain anatomy in two separate
742 experiments with horizonal and sagittal brain sections. Panel A-B: Overlay of nine segmented ROIs
743 generated from UMAP and K-mean clustering analysis in horizonal hemisphere sections (A) and sagittal
744 brain sections (B). Panel C-D: Scatterplot of UMAP first 2 components (V1 vs V2) projecting the
745 distribution and similarity of 9 segmented ROIs in horizonal (C) and sagittal sections (D). See Table S4
746 for the list of 5 LPEs.

747

748 **References**

749


750 1. Shimma, S. (2022). Mass Spectrometry Imaging. Mass Spectrom (Tokyo) *11*, A0102.
751 10.5702/massspectrometry.A0102.
752 2. Zhang, H., Delafield, D.G., and Li, L. (2023). Mass spectrometry imaging: the rise of spatially resolved
753 single-cell omics. Nat Methods *20*, 327-330. 10.1038/s41592-023-01774-6.
754 3. Zhang, L., Liang, X., Takac, T., Komis, G., Li, X., Zhang, Y., Ovecka, M., Chen, Y., and Samaj, J. (2023).
755 Spatial proteomics of vesicular trafficking: coupling mass spectrometry and imaging approaches in
756 membrane biology. Plant Biotechnol J *21*, 250-269. 10.1111/pbi.13929.
757 4. Wang, J., Zhao, J., Nie, S., Xie, M., and Li, S. (2023). MALDI mass spectrometry in food carbohydrates
758 analysis: A review of recent researches. Food Chem *399*, 133968. 10.1016/j.foodchem.2022.133968.
759 5. Soudah, T., Zoabi, A., and Margulis, K. (2023). Desorption electrospray ionization mass spectrometry
760 imaging in discovery and development of novel therapies. Mass Spectrom Rev *42*, 751-778.
761 10.1002/mas.21736.
762 6. Sivanesan, I., Gopal, J., Hasan, N., and Muthu, M. (2023). A systematic assessment of matrix-assisted
763 laser desorption/ionization time of flight mass spectrometry (MALDI-TOF MS) application for rapid
764 identification of pathogenic microbes that affect food crops: delivered and future deliverables. RSC Adv
765 *13*, 17297-17314. 10.1039/d3ra01633a.
766 7. Roncevic, A., Koruga, N., Soldo Koruga, A., Debeljak, Z., Roncevic, R., Turk, T., Kretic, D., Rotim, T., Krivdic
767 Dupan, Z., Troha, D., et al. (2023). MALDI Imaging Mass Spectrometry of High-Grade Gliomas: A Review
768 of Recent Progress and Future Perspective. Curr Issues Mol Biol *45*, 838-851. 10.3390/cimb45020055.
769 8. Moore, J.L., Patterson, N.H., Norris, J.L., and Caprioli, R.M. (2023). Prospective on Imaging Mass
770 Spectrometry in Clinical Diagnostics. Mol Cell Proteomics, 100576. 10.1016/j.mcpro.2023.100576.
771 9. Liu, J., Hu, W., Han, Y., and Nie, H. (2023). Recent advances in mass spectrometry imaging of single cells.
772 Anal Bioanal Chem *415*, 4093-4110. 10.1007/s00216-023-04774-9.

773 10. Li, D., Ouyang, Z., and Ma, X. (2023). Mass Spectrometry Imaging for Single-Cell or Subcellular
774 Lipidomics: A Review of Recent Advancements and Future Development. Molecules *28*.
775 10.3390/molecules28062712.
776 11. Jiang, L.X., Yang, M., Wali, S.N., and Laskin, J. (2023). High-Throughput Mass Spectrometry Imaging of
777 Biological Systems: Current Approaches and Future Directions. Trends Analyt Chem *163*.
778 10.1016/j.trac.2023.117055.
779 12. Ikegawa, M., Kakuda, N., Miyasaka, T., Toyama, Y., Nirasawa, T., Minta, K., and Hanrieder, J. (2023).
780 Mass Spectrometry Imaging in Alzheimer's Disease. Brain Connect. 10.1089/brain.2022.0057.
781 13. Gorman, B.L., Torti, S.V., Torti, F.M., and Anderton, C.R. (2023). Mass spectrometry imaging of metals in
782 tissues and cells: Methods and biological applications. Biochim Biophys Acta Gen Subj, 130329.
783 10.1016/j.bbagen.2023.130329.
784 14. Gitta, S., Mark, L., Szentpeteri, J.L., and Szabo, E. (2023). Lipid Changes in the Peri-Implantation Period
785 with Mass Spectrometry Imaging: A Systematic Review. Life (Basel) *13*. 10.3390/life13010169.
786 15. Zou, Y., Tang, W., and Li, B. (2022). Mass spectrometry imaging and its potential in food microbiology.
787 Int J Food Microbiol *371*, 109675. 10.1016/j.ijfoodmicro.2022.109675.
788 16. Zhao, Z., Ding, Y., Tran, L.J., Chai, G., and Lin, L. (2023). Innovative breakthroughs facilitated by single-cell
789 multi-omics: manipulating natural killer cell functionality correlates with a novel subcategory of
790 melanoma cells. Front Immunol *14*, 1196892. 10.3389/fimmu.2023.1196892.
791 17. Vos, D.R.N., Ellis, S.R., Balluff, B., and Heeren, R.M.A. (2021). Experimental and Data Analysis
792 Considerations for Three-Dimensional Mass Spectrometry Imaging in Biomedical Research. Mol Imaging
793 Biol *23*, 149-159. 10.1007/s11307-020-01541-5.
794 18. Verbeeck, N., Caprioli, R.M., and Van de Plas, R. (2020). Unsupervised machine learning for exploratory
795 data analysis in imaging mass spectrometry. Mass Spectrom Rev *39*, 245-291. 10.1002/mas.21602.
796 19. Alexandrov, T. (2012). MALDI imaging mass spectrometry: statistical data analysis and current
797 computational challenges. BMC Bioinformatics *13 Suppl 16*, S11. 10.1186/1471-2105-13-S16-S11.
798 20. Trede, D., Kobarg, J.H., Oetjen, J., Thiele, H., Maass, P., and Alexandrov, T. (2012). On the importance of
799 mathematical methods for analysis of MALDI-imaging mass spectrometry data. J Integr Bioinform *9*, 189.
800 10.2390/biecoll-jib-2012-189.
801 21. Riches, S.F., Payne, G.S., Morgan, V.A., Sandhu, S., Fisher, C., Germuska, M., Collins, D.J., Thompson, A.,
802 and deSouza, N.M. (2009). MRI in the detection of prostate cancer: combined apparent diffusion
803 coefficient, metabolite ratio, and vascular parameters. AJR Am J Roentgenol *193*, 1583-1591.
804 10.2214/AJR.09.2540.
805 22. Jia, F., Zhao, X., and Zhao, Y. (2023). Advancements in ToF-SIMS imaging for life sciences. Front Chem *11*,
806 1237408. 10.3389/fchem.2023.1237408.
807 23. Pumphrey, G.M., Hanson, B.T., Chandra, S., and Madsen, E.L. (2009). Dynamic secondary ion mass
808 spectrometry imaging of microbial populations utilizing C-labelled substrates in pure culture and in soil.
809 Environ Microbiol *11*, 220-229. 10.1111/j.1462-2920.2008.01757.x.
810 24. Suhre, K., Wallaschofski, H., Raffler, J., Friedrich, N., Haring, R., Michael, K., Wasner, C., Krebs, A.,
811 Kronenberg, F., Chang, D., et al. (2011). A genome-wide association study of metabolic traits in human
812 urine. Nat Genet *43*, 565-569. 10.1038/ng.837.
813 25. Illig, T., Gieger, C., Zhai, G., Romisch-Margl, W., Wang-Sattler, R., Prehn, C., Altmaier, E., Kastenmuller,
814 G., Kato, B.S., Mewes, H.W., et al. (2010). A genome-wide perspective of genetic variation in human
815 metabolism. Nat Genet *42*, 137-141. 10.1038/ng.507.
816 26. Gieger, C., Geistlinger, L., Altmaier, E., Hrabe de Angelis, M., Kronenberg, F., Meitinger, T., Mewes, H.W.,
817 Wichmann, H.E., Weinberger, K.M., Adamski, J., et al. (2008). Genetics meets metabolomics: a genome-
818 wide association study of metabolite profiles in human serum. PLoS Genet *4*, e1000282.
819 10.1371/journal.pgen.1000282.

820 27. Petersen, A.K., Krumsiek, J., Wagele, B., Theis, F.J., Wichmann, H.E., Gieger, C., and Suhre, K. (2012). On
821 the hypothesis-free testing of metabolite ratios in genome-wide and metabolome-wide association
822 studies. BMC Bioinformatics *13*, 120. 10.1186/1471-2105-13-120.
823 28. Lassen, J.K., Wang, T., Nielsen, K.L., Hasselstrom, J.B., Johannsen, M., and Villesen, P. (2023). Large-Scale
824 metabolomics: Predicting biological age using 10,133 routine untargeted LC-MS measurements. Aging
825 Cell *22*, e13813. 10.1111/acel.13813.
826 29. Schramm, T., Hester, Z., Klinkert, I., Both, J.P., Heeren, R.M.A., Brunelle, A., Laprevote, O., Desbenoit, N.,
827 Robbe, M.F., Stoeckli, M., et al. (2012). imzML--a common data format for the flexible exchange and
828 processing of mass spectrometry imaging data. J Proteomics *75*, 5106-5110.
829 10.1016/j.jprot.2012.07.026.
830 30. Pang, Z., Zhou, G., Ewald, J., Chang, L., Hacariz, O., Basu, N., and Xia, J. (2022). Using MetaboAnalyst 5.0
831 for LC-HRMS spectra processing, multi-omics integration and covariate adjustment of global
832 metabolomics data. Nat Protoc *17*, 1735-1761. 10.1038/s41596-022-00710-w.
833 31. Thompson, P.T., and Moseley, H.N.B. (2023). MESSES: Software for Transforming Messy Research
834 Datasets into Clean Submissions to Metabolomics Workbench for Public Sharing. Metabolites *13*.
835 10.3390/metabo13070842.
836 32. Powell, C.D., and Moseley, H.N.B. (2023). The metabolomics workbench file status website: a metadata
837 repository promoting FAIR principles of metabolomics data. BMC Bioinformatics *24*, 299.
838 10.1186/s12859-023-05423-9.
839 33. Sud, M., Fahy, E., Cotter, D., Azam, K., Vadivelu, I., Burant, C., Edison, A., Fiehn, O., Higashi, R., Nair, K.S.,
840 et al. (2016). Metabolomics Workbench: An international repository for metabolomics data and
841 metadata, metabolite standards, protocols, tutorials and training, and analysis tools. Nucleic Acids Res
842 *44*, D463-470. 10.1093/nar/gkv1042.
843 34. Rodeiro, J., Vidana-Vila, E., Navarro, J., and Mallol, R. (2023). CloMet: A Novel Open-Source and Modular
844 Software Platform That Connects Established Metabolomics Repositories and Data Analysis Resources. J
845 Proteome Res *22*, 2540-2547. 10.1021/acs.jproteome.2c00602.
846 35. Du, X., Dastmalchi, F., Ye, H., Garrett, T.J., Diller, M.A., Liu, M., Hogan, W.R., Brochhausen, M., and
847 Lemas, D.J. (2023). Evaluating LC-HRMS metabolomics data processing software using FAIR principles for
848 research software. Metabolomics *19*, 11. 10.1007/s11306-023-01974-3.
849 36. Dekermanjian, J., Labeikovsky, W., Ghosh, D., and Kechris, K. (2021). MSCAT: A Machine Learning
850 Assisted Catalog of Metabolomics Software Tools. Metabolites *11*. 10.3390/metabo11100678.
851 37. Plyushchenko, I.V., Fedorova, E.S., Potoldykova, N.V., Polyakovskiy, K.A., Glukhov, A.I., and Rodin, I.A.
852 (2022). Omics Untargeted Key Script: R-Based Software Toolbox for Untargeted Metabolomics with
853 Bladder Cancer Biomarkers Discovery Case Study. J Proteome Res *21*, 833-847.
854 10.1021/acs.jproteome.1c00392.
855 38. Misra, B.B. (2021). New software tools, databases, and resources in metabolomics: updates from 2020.
856 Metabolomics *17*, 49. 10.1007/s11306-021-01796-1.
857 39. Chang, H.Y., Colby, S.M., Du, X., Gomez, J.D., Helf, M.J., Kechris, K., Kirkpatrick, C.R., Li, S., Patti, G.J.,
858 Renslow, R.S., et al. (2021). A Practical Guide to Metabolomics Software Development. Anal Chem *93*,
859 1912-1923. 10.1021/acs.analchem.0c03581.
860 40. O'Shea, K., and Misra, B.B. (2020). Software tools, databases and resources in metabolomics: updates
861 from 2018 to 2019. Metabolomics *16*, 36. 10.1007/s11306-020-01657-3.
862 41. Adams, K.J., Pratt, B., Bose, N., Dubois, L.G., St John-Williams, L., Perrott, K.M., Ky, K., Kapahi, P., Sharma,
863 V., MacCoss, M.J., et al. (2020). Skyline for Small Molecules: A Unifying Software Package for
864 Quantitative Metabolomics. J Proteome Res *19*, 1447-1458. 10.1021/acs.jproteome.9b00640.
865 42. Misra, B.B. (2020). Open-Source Software Tools, Databases, and Resources for Single-Cell and Single-
866 Cell-Type Metabolomics. Methods Mol Biol *2064*, 191-217. 10.1007/978-1-4939-9831-9_15.

43. Shahjaman, M., Rahman, M.R., Islam, T., Auwul, M.R., Moni, M.A., and Mollah, M.N.H. (2021). rMisbeta: A robust missing value imputation approach in transcriptomics and metabolomics data. Comput Biol Med *138*, 104911. 10.1016/j.compbiomed.2021.104911.
44. Wei, R., Wang, J., Su, M., Jia, E., Chen, S., Chen, T., and Ni, Y. (2018). Missing Value Imputation Approach for Mass Spectrometry-based Metabolomics Data. Sci Rep *8*, 663. 10.1038/s41598-017-19120-0.
45. Jin, Z., Kang, J., and Yu, T. (2018). Missing value imputation for LC-MS metabolomics data by incorporating metabolic network and adduct ion relations. Bioinformatics *34*, 1555-1561. 10.1093/bioinformatics/btx816.
46. Di Guida, R., Engel, J., Allwood, J.W., Weber, R.J., Jones, M.R., Sommer, U., Viant, M.R., and Dunn, W.B. (2016). Non-targeted UHPLC-MS metabolomic data processing methods: a comparative investigation of normalisation, missing value imputation, transformation and scaling. Metabolomics *12*, 93. 10.1007/s11306-016-1030-9.
47. Rieppo, J., Hyttinen, M.M., Jurvelin, J.S., and Helminen, H.J. (2004). Reference sample method reduces the error caused by variable cryosection thickness in Fourier transform infrared imaging. Appl Spectrosc *58*, 137-140. 10.1366/000370204322729577.
48. Lu, W., Park, N.R., TeSlaa, T., Jankowski, C.S.R., Samarah, L., McReynolds, M., Xing, X., Schembri, J., Woolf, M.T., Rabinowitz, J.D., and Davidson, S.M. (2023). Acidic Methanol Treatment Facilitates Matrix-Assisted Laser Desorption Ionization-Mass Spectrometry Imaging of Energy Metabolism. Anal Chem *95*, 14879-14888. 10.1021/acs.analchem.3c01875.
49. Knecht, K., Wiesmuller, K.H., Gnau, V., Jung, G., Meyermann, R., Todd, K.G., and Hamprecht, B. (2001). AMP deaminase in rat brain: localization in neurons and ependymal cells. J Neurosci Res *66*, 941-950. 10.1002/jnr.10059.
50. Andruchow, N.D., Konishi, K., Shatenstein, B., and Bohbot, V.D. (2017). A lower ratio of omega-6 to omega-3 fatty acids predicts better hippocampus-dependent spatial memory and cognitive status in older adults. Neuropsychology *31*, 724-734. 10.1037/neu0000373.
51. Southwell, N., Primiano, G., Nadkarni, V., Attarwala, N., Beattie, E., Miller, D., Alam, S., Liparulo, I., Shurubor, Y.I., Valentino, M.L., et al. (2023). A coordinated multiorgan metabolic response contributes to human mitochondrial myopathy. EMBO Mol Med *15*, e16951. 10.15252/emmm.202216951.
52. Bakker, N., Hickey, M., Shams, R., Rivera, C.F., Vlahos, J., Cense, H.A., Demirkiran, A., Ramkhelawon, B., and Houdijk, A.P. (2023). Oral omega-3 PUFA supplementation modulates inflammation in adipose tissue depots in morbidly obese women: A randomized trial. Nutrition *111*, 112055. 10.1016/j.nut.2023.112055.
53. Pinel, A., Rigaudiere, J.P., Morio, B., and Capel, F. (2021). Adipose Tissue Dysfunctions in Response to an Obesogenic Diet Are Reduced in Mice after Transgenerational Supplementation with Omega 3 Fatty Acids. Metabolites *11*. 10.3390/metabo11120838.
54. Portela, N.D., Galvan, C., Sanmarco, L.M., Bergero, G., Aoki, M.P., Cano, R.C., and Pesoa, S.A. (2023). Omega-3-Supplemented Fat Diet Drives Immune Metabolic Response in Visceral Adipose Tissue by Modulating Gut Microbiota in a Mouse Model of Obesity. Nutrients *15*. 10.3390/nu15061404.
55. Wall, R., Ross, R.P., Shanahan, F., O'Mahony, L., O'Mahony, C., Coakley, M., Hart, O., Lawlor, P., Quigley, E.M., Kiely, B., et al. (2009). Metabolic activity of the enteric microbiota influences the fatty acid composition of murine and porcine liver and adipose tissues. Am J Clin Nutr *89*, 1393-1401. 10.3945/ajcn.2008.27023.
56. Chiusolo, S., Bork, C.S., Gentile, F., Lundbye-Christensen, S., Harris, W.S., Schmidt, E.B., and De Caterina, R. (2023). Adipose tissue n-3/n-6 fatty acids ratios versus n-3 fatty acids fractions as predictors of myocardial infarction. Am Heart J *262*, 38-48. 10.1016/j.ahj.2023.03.019.
57. Rix, T.A., Dinesen, P., Lundbye-Christensen, S., Joensen, A.M., Riahi, S., Overvad, K., and Schmidt, E.B. (2022). Omega-3 fatty acids in adipose tissue and risk of atrial fibrillation. Eur J Clin Invest *52*, e13649. 10.1111/eci.13649.

58. Hertz, L., and Rothman, D.L. (2017). Glutamine-Glutamate Cycle Flux Is Similar in Cultured Astrocytes and Brain and Both Glutamate Production and Oxidation Are Mainly Catalyzed by Aspartate Aminotransferase. Biology (Basel) *6*. 10.3390/biology6010017.
59. Andersen, J.V., Schousboe, A., and Verkhratsky, A. (2022). Astrocyte energy and neurotransmitter metabolism in Alzheimer's disease: Integration of the glutamate/GABA-glutamine cycle. Prog Neurobiol *217*, 102331. 10.1016/j.pneurobio.2022.102331.
60. Pardo, B., Rodrigues, T.B., Contreras, L., Garzon, M., Llorente-Folch, I., Kobayashi, K., Saheki, T., Cerdan, S., and Satrustegui, J. (2011). Brain glutamine synthesis requires neuronal-born aspartate as amino donor for glial glutamate formation. J Cereb Blood Flow Metab *31*, 90-101. 10.1038/jcbfm.2010.146.
61. Szerb, J.C., and O'Regan, P.A. (1985). Effect of glutamine on glutamate release from hippocampal slices induced by high K+ or by electrical stimulation: interaction with different Ca2+ concentrations. J Neurochem *44*, 1724-1731. 10.1111/j.1471-4159.1985.tb07160.x.
62. Kantorova, E., Hnilicova, P., Bogner, W., Grendar, M., Grossmann, J., Kovacova, S., Heckova, E., Strasser, B., Cierny, D., Zelenak, K., and Kurca, E. (2022). Neurocognitive performance in relapsing-remitting multiple sclerosis patients is associated with metabolic abnormalities of the thalamus but not the hippocampus- GABA-edited 1H MRS study. Neurol Res *44*, 57-64. 10.1080/01616412.2021.1956282.
63. Kantorova, E., Hnilicova, P., Bogner, W., Grendar, M., Cierny, D., Heckova, E., Strasser, B., Ruzinak, R., Zelenak, K., and Kurca, E. (2021). Positivity of oligoclonal bands in the cerebrospinal fluid predisposed to metabolic changes and rearrangement of inhibitory/excitatory neurotransmitters in subcortical brain structures in multiple sclerosis. Mult Scler Relat Disord *52*, 102978. 10.1016/j.msard.2021.102978.
64. Limon, I.D., Angulo-Cruz, I., Sanchez-Abdon, L., and Patricio-Martinez, A. (2021). Disturbance of the Glutamate-Glutamine Cycle, Secondary to Hepatic Damage, Compromises Memory Function. Front Neurosci *15*, 578922. 10.3389/fnins.2021.578922.
65. Hangel, G., Cadrien, C., Lazen, P., Furtner, J., Lipka, A., Heckova, E., Hingerl, L., Motyka, S., Gruber, S., Strasser, B., et al. (2020). High-resolution metabolic imaging of high-grade gliomas using 7T-CRT-FID-MRSI. Neuroimage Clin *28*, 102433. 10.1016/j.nicl.2020.102433.
66. Yu, J., Guo, Y., Sun, M., Li, B., Zhang, Y., and Li, C. (2009). Iron is a potential key mediator of glutamate excitotoxicity in spinal cord motor neurons. Brain Res *1257*, 102-107. 10.1016/j.brainres.2008.12.030.
67. Burger, A., Kotze, M.J., Stein, D.J., Janse van Rensburg, S., and Howells, F.M. (2020). The relationship between measurement of in vivo brain glutamate and markers of iron metabolism: A proton magnetic resonance spectroscopy study in healthy adults. Eur J Neurosci *51*, 984-990. 10.1111/ejn.14583.
68. Peng Yu1, Ming Zhang1,2#, Hui Ding1, Xiaojing Di1, Peng Guan2, Shumin Wang1, Zhenhua Shi1, Dongyun Jiang1,2, Xianglin Duan1,2* and Yan-Zhong Chang1,2 (2015). Effect of Glutamate on Brain Iron Metabolism and the Regulation Mechanism. Journal of Drug Metabolism & Toxicology *6*, 1-10. 10.4172/2157-7609.1000190.
69. McGahan, M.C., Harned, J., Mukunnemkeril, M., Goralska, M., Fleisher, L., and Ferrell, J.B. (2005). Iron alters glutamate secretion by regulating cytosolic aconitase activity. Am J Physiol Cell Physiol *288*, C1117-1124. 10.1152/ajpcell.00444.2004.
70. Mittal, R.D., Pandey, A., Mittal, B., and Agarwal, K.N. (2003). Effect of latent iron deficiency on GABA and glutamate neuroreceptors in rat brain. Indian J Clin Biochem *18*, 111-116. 10.1007/BF02867677.
71. Sato, T., Shapiro, J.S., Chang, H.C., Miller, R.A., and Ardehali, H. (2022). Aging is associated with increased brain iron through cortex-derived hepcidin expression. Elife *11*. 10.7554/eLife.73456.
72. Wei, S., Shi, W., Li, M., and Gao, Q. (2014). Calorie restriction down-regulates expression of the iron regulatory hormone hepcidin in normal and D-galactose-induced aging mouse brain. Rejuvenation Res *17*, 19-26. 10.1089/rej.2013.1450.
73. Guo, A., Chen, Z., Li, F., and Luo, Q. (2022). Delineating regions of interest for mass spectrometry imaging by multimodally corroborated spatial segmentation. Gigascience *12*. 10.1093/gigascience/giad021.

963 74. Shi, W., Bell, S., Iyer, H., Brenden, C.K., Zhang, Y., Kim, S., Park, I., Bashir, R., Sweedler, J., and Vlasov, Y.
964 (2022). Integrated silicon microfluidic chip for picoliter-scale analyte segmentation and microscale
965 printing for mass spectrometry imaging. Lab Chip *23*, 72-80. 10.1039/d2lc00688j.
966 75. Guo, L., Liu, X., Zhao, C., Hu, Z., Xu, X., Cheng, K.K., Zhou, P., Xiao, Y., Shah, M., Xu, J., et al. (2022).
967 iSegMSI: An Interactive Strategy to Improve Spatial Segmentation of Mass Spectrometry Imaging Data.
968 Anal Chem *94*, 14522-14529. 10.1021/acs.analchem.2c01456.
969 76. Zou, Y., Tang, W., and Li, B. (2023). Spatial segmentation of mass spectrometry imaging data featuring
970 selected principal components. Talanta *253*, 123958. 10.1016/j.talanta.2022.123958.
971 77. Baars, M.J.D., Sinha, N., Amini, M., Pieterman-Bos, A., van Dam, S., Ganpat, M.M.P., Lacle, M.M.,
972 Oldenburg, B., and Vercoulen, Y. (2021). MATISSE: a method for improved single cell segmentation in
973 imaging mass cytometry. BMC Biol *19*, 99. 10.1186/s12915-021-01043-y.
974 78. Guo, L., Hu, Z., Zhao, C., Xu, X., Wang, S., Xu, J., Dong, J., and Cai, Z. (2021). Data Filtering and Its
975 Prioritization in Pipelines for Spatial Segmentation of Mass Spectrometry Imaging. Anal Chem *93*, 4788-
976 4793. 10.1021/acs.analchem.0c05242.
977 79. Hu, H., Yin, R., Brown, H.M., and Laskin, J. (2021). Spatial Segmentation of Mass Spectrometry Imaging
978 Data by Combining Multivariate Clustering and Univariate Thresholding. Anal Chem *93*, 3477-3485.
979 10.1021/acs.analchem.0c04798.
980 80. Rothman, D.L., Behar, K.L., Prichard, J.W., and Petroff, O.A. (1997). Homocarnosine and the
981 measurement of neuronal pH in patients with epilepsy. Magn Reson Med *38*, 924-929.
982 10.1002/mrm.1910380611.
983 81. Filipovic, D., Ivetic, V., Bozic, K., Nikolic, V., and Naumovic, N. (1993). [The effect of homocarnosine on
984 neuronal activity during satiation and starvation]. Med Pregl *46*, 393-397.
985 82. Bondarenko, T.I., Krichevskaia, A.A., and Koshchii, G.N. (1985). [Homocarnosine in the brain of rats
986 during cold adaptation]. Fiziol Zh SSSR Im I M Sechenova *71*, 333-336.
987 83. Kukharenko, R.I., Reva, A.D., and Rodina, S.L. (1990). [An increase in the brain homocarnosine level
988 during alcohol intoxication]. Ukr Biokhim Zh (1978) *62*, 92-94.
989 84. Jalil, M.A., Begum, L., Contreras, L., Pardo, B., Iijima, M., Li, M.X., Ramos, M., Marmol, P., Horiuchi, M.,
990 Shimotsu, K., et al. (2005). Reduced N-acetylaspartate levels in mice lacking aralar, a brain- and muscle-
991 type mitochondrial aspartate-glutamate carrier. J Biol Chem *280*, 31333-31339.
992 10.1074/jbc.M505286200.
993 85. Ohtsuka, C., and Takahashi, H. (1983). Brain function estimated from the ratio of glutamine to
994 homocarnosine levels in cerebrospinal fluid. Brain Dev *5*, 509-511. 10.1016/s0387-7604(83)80084-9.
995 86. Enwonwu, C.O., and Worthington, B.S. (1973). Accumulation of histidine, 3-methylhistidine, and
996 homocarnosine in the brains of protein-calorie deficient monkeys. J Neurochem *21*, 799-807.
997 10.1111/j.1471-4159.1973.tb07524.x.
998 87. Rather, A.A., and Chachoo, M.A. (2023). Robust correlation estimation and UMAP assisted topological
999 analysis of omics data for disease subtyping. Comput Biol Med *155*, 106640.
1000 10.1016/j.compbiomed.2023.106640.
1001 88. ElKarami, B., Alkhateeb, A., Qattous, H., Alshomali, L., and Shahrrava, B. (2022). Multi-omics Data
1002 Integration Model Based on UMAP Embedding and Convolutional Neural Network. Cancer Inform *21*,
1003 11769351221124205. 10.1177/11769351221124205.
1004 89. Do, V.H., and Canzar, S. (2021). A generalization of t-SNE and UMAP to single-cell multimodal omics.
1005 Genome Biol *22*, 130. 10.1186/s13059-021-02356-5.
1006 90. Kharel, P., Singhal, N.K., Mahendran, T., West, N., Croos, B., Rana, J., Smith, L., Freeman, E.,
1007 Chattopadhyay, A., McDonough, J., and Basu, S. (2023). NAT8L mRNA oxidation is linked to
1008 neurodegeneration in multiple sclerosis. Cell Chem Biol *30*, 308-320 e305.
1009 10.1016/j.chembiol.2023.02.007.

1010 91. Uno, K., Miyanishi, H., Sodeyama, K., Fujiwara, T., Miyazaki, T., Muramatsu, S.I., and Nitta, A. (2019).
1011 Vulnerability to depressive behavior induced by overexpression of striatal Shati/Nat8l via the
1012 serotonergic neuronal pathway in mice. Behav Brain Res *376*, 112227. 10.1016/j.bbr.2019.112227.
1013 92. Morland, C., and Nordengen, K. (2022). N-Acetyl-Aspartyl-Glutamate in Brain Health and Disease. Int J
1014 Mol Sci *23*. 10.3390/ijms23031268.

1015

**Figure 1**

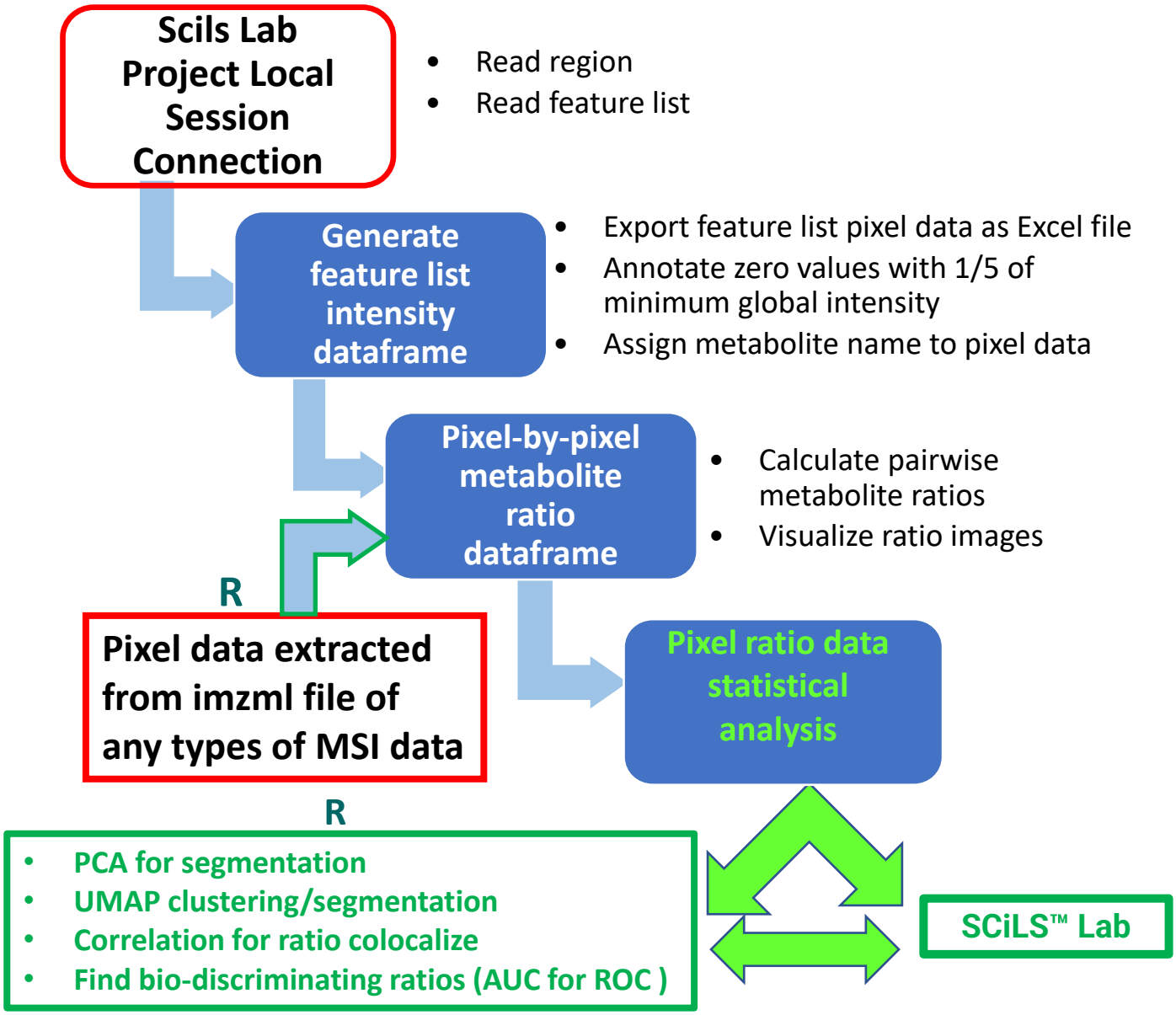
Scils Lab Project Local Session Connection
Read region
Read feature list
Generate feature list intensity dataframe
Export feature list pixel data as Excel file
Annotate zero values with 1/5 of minimum global intensity
Assign metabolite name to pixel data
Pixel-by-pixel metabolite ratio dataframe
Calculate pairwise metabolite ratios
Visualize ratio images
R
Pixel data extracted from imzml file of any types of MSI data
Pixel ratio data statistical analysis
R
PCA for segmentation
UMAP clustering/segmentation
Correlation for ratio colocalize
Find bio-discriminating ratios (AUC for ROC )
SCiLS™ Lab

# Figure 2

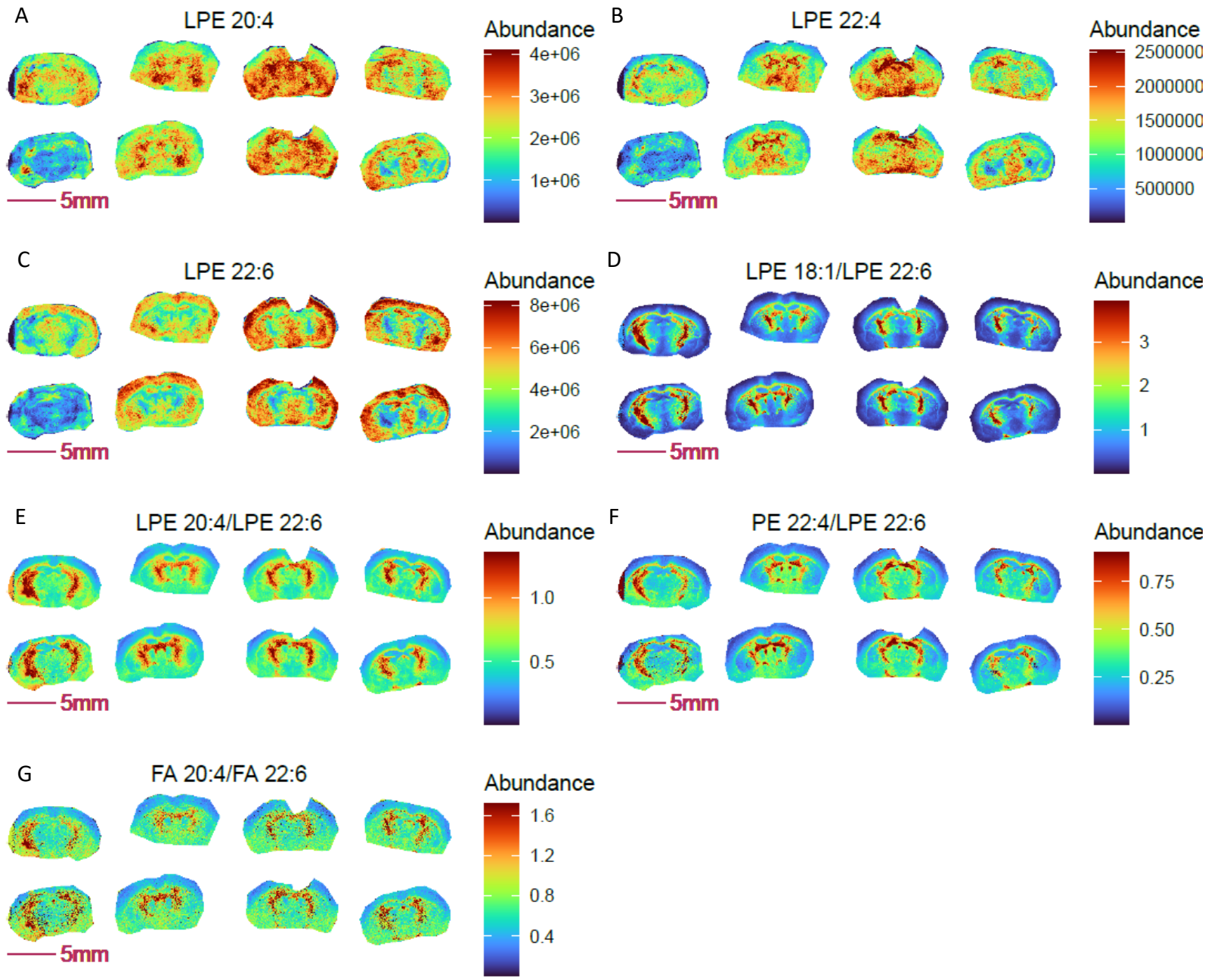
A
LPE 20:4
Abundance
4e+06
3e+06
2e+06
1e+06
5mm
B
LPE 22:4
Abundance
2500000
2000000
1500000
1000000
500000
5mm
C
LPE 22:6
Abundance
8e+06
6e+06
4e+06
2e+06
5mm
D
LPE 18:1/LPE 22:6
Abundance
3
2
1
5mm
E
LPE 20:4/LPE 22:6
Abundance
1.0
0.5
5mm
F
PE 22:4/LPE 22:6
Abundance
0.75
0.50
0.25
5mm
G
FA 20:4/FA 22:6
Abundance
1.6
1.2
0.8
0.4
5mm

# Figure 3

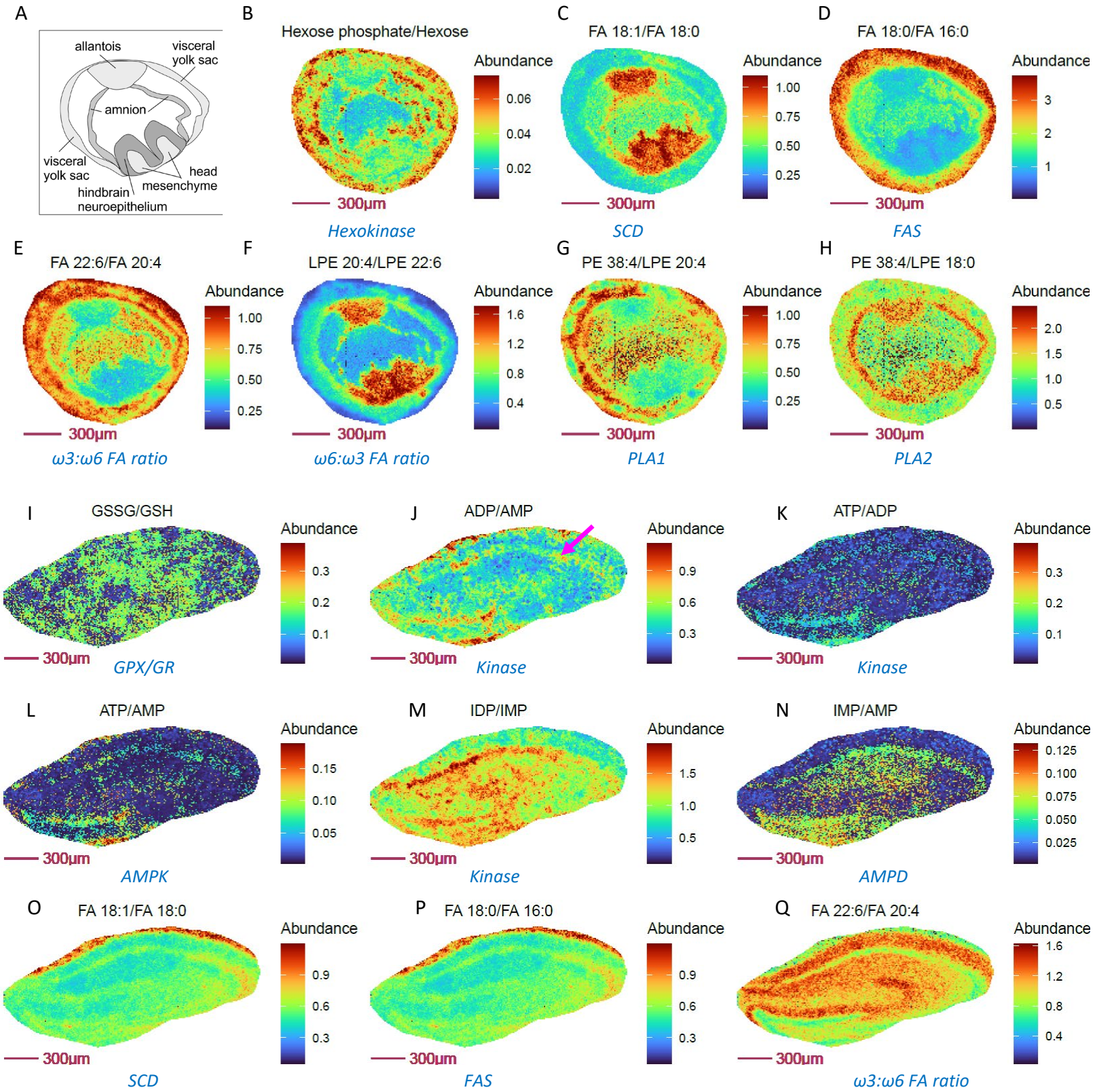
A
allantois
visceral yolk sac
amnion
visceral yolk sac
head mesenchyme
hindbrain neuroepithelium
B
Hexose phosphate/Hexose
Abundance
0.06
0.04
0.02
300µm
Hexokinase
C
FA 18:1/FA 18:0
Abundance
1.00
0.75
0.50
0.25
300µm
SCD
D
FA 18:0/FA 16:0
Abundance
3
2
1
300µm
FAS
E
FA 22:6/FA 20:4
Abundance
1.00
0.75
0.50
0.25
300µm
ω3:ω6 FA ratio
F
LPE 20:4/LPE 22:6
Abundance
1.6
1.2
0.8
0.4
300µm
ω6:ω3 FA ratio
G
PE 38:4/LPE 20:4
Abundance
1.00
0.75
0.50
0.25
300µm
PLA1
H
PE 38:4/LPE 18:0
Abundance
2.0
1.5
1.0
0.5
300µm
PLA2
I
GSSG/GSH
Abundance
0.3
0.2
0.1
300µm
GPX/GR
J
ADP/AMP
Abundance
0.9
0.6
0.3
300µm
Kinase
K
ATP/ADP
Abundance
0.3
0.2
0.1
300µm
Kinase
L
ATP/AMP
Abundance
0.15
0.10
0.05
300µm
AMPK
M
IDP/IMP
Abundance
1.5
1.0
0.5
300µm
Kinase
N
IMP/AMP
Abundance
0.125
0.100
0.075
0.050
0.025
300µm
AMPD
O
FA 18:1/FA 18:0
Abundance
0.9
0.6
0.3
300µm
SCD
P
FA 18:0/FA 16:0
Abundance
0.9
0.6
0.3
300µm
FAS
Q
FA 22:6/FA 20:4
Abundance
1.6
1.2
0.8
0.4
300µm
ω3:ω6 FA ratio

# Figure 4

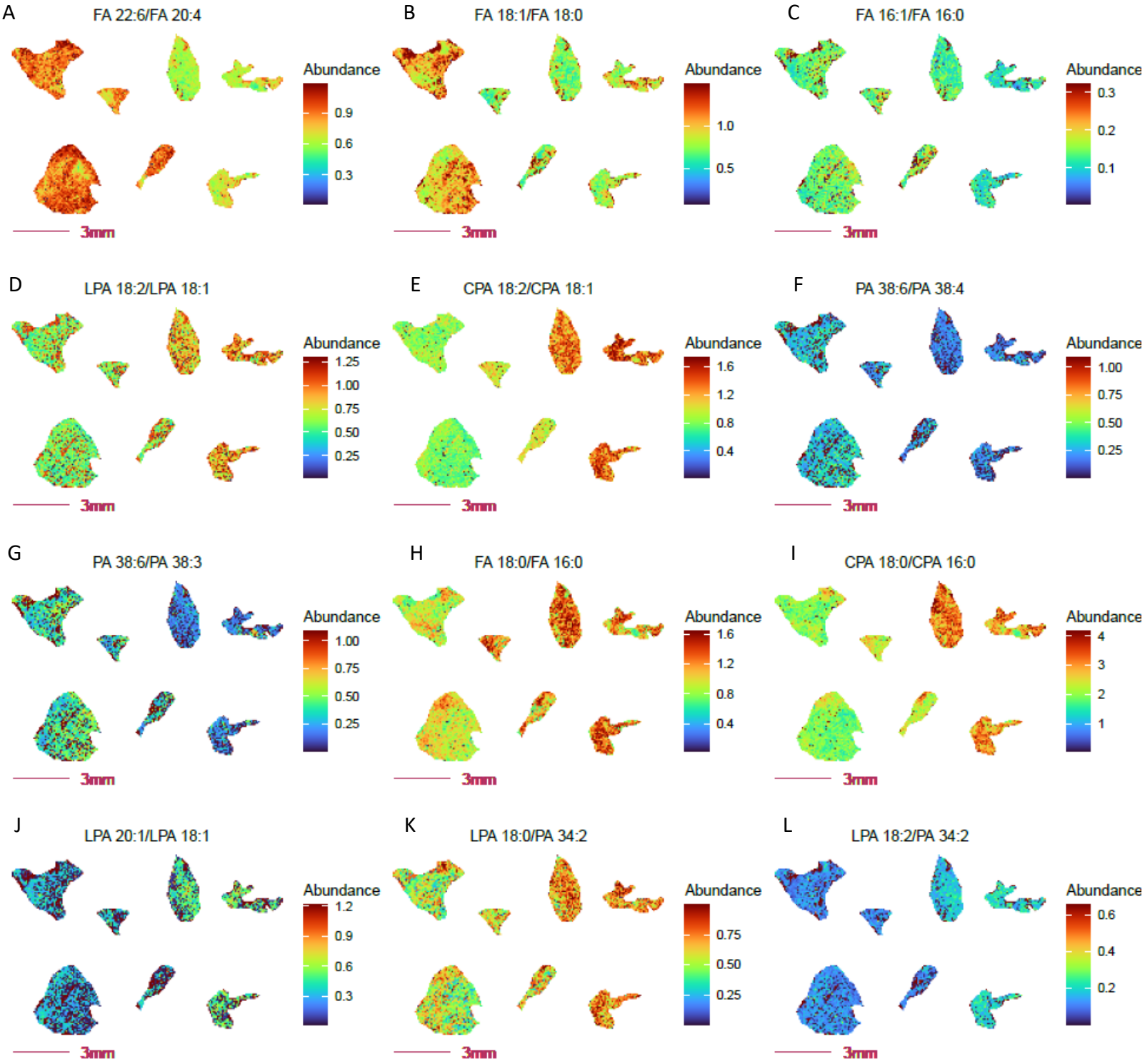
A
FA 22:6/FA 20:4
Abundance
0.9
0.6
0.3
3mm
B
FA 18:1/FA 18:0
Abundance
1.0
0.5
3mm
C
FA 16:1/FA 16:0
Abundance
0.3
0.2
0.1
3mm
D
LPA 18:2/LPA 18:1
Abundance
1.25
1.00
0.75
0.50
0.25
3mm
E
CPA 18:2/CPA 18:1
Abundance
1.6
1.2
0.8
0.4
3mm
F
PA 38:6/PA 38:4
Abundance
1.00
0.75
0.50
0.25
3mm
G
PA 38:6/PA 38:3
Abundance
1.00
0.75
0.50
0.25
3mm
H
FA 18:0/FA 16:0
Abundance
1.6
1.2
0.8
0.4
3mm
I
CPA 18:0/CPA 16:0
Abundance
4
3
2
1
3mm
J
LPA 20:1/LPA 18:1
Abundance
1.2
0.9
0.6
0.3
3mm
K
LPA 18:0/PA 34:2
Abundance
0.75
0.50
0.25
3mm
L
LPA 18:2/PA 34:2
Abundance
0.6
0.4
0.2
3mm

# Figure 5

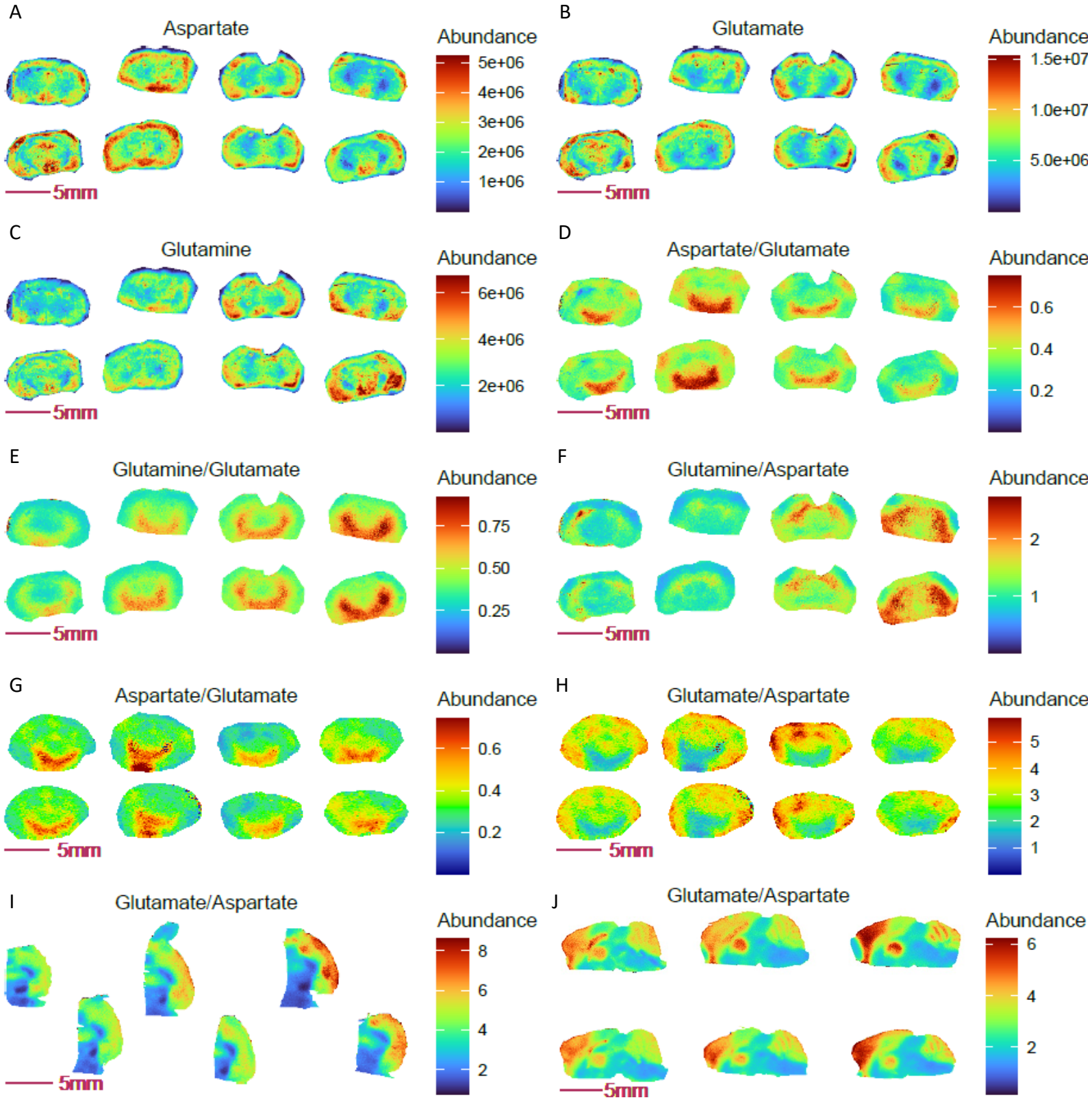
A
Aspartate
Abundance
5e+06
4e+06
3e+06
2e+06
1e+06
5mm
B
Glutamate
Abundance
1.5e+07
1.0e+07
5.0e+06
5mm
C
Glutamine
Abundance
6e+06
4e+06
2e+06
5mm
D
Aspartate/Glutamate
Abundance
0.6
0.4
0.2
5mm
E
Glutamine/Glutamate
Abundance
0.75
0.50
0.25
5mm
F
Glutamine/Aspartate
Abundance
2
1
5mm
G
Aspartate/Glutamate
Abundance
0.6
0.4
0.2
5mm
H
Glutamate/Aspartate
Abundance
5
4
3
2
1
5mm
I
Glutamate/Aspartate
Abundance
8
6
4
2
5mm
J
Glutamate/Aspartate
Abundance
6
4
2
5mm

**Figure 6**

A **10 Glutamate Metabolites**

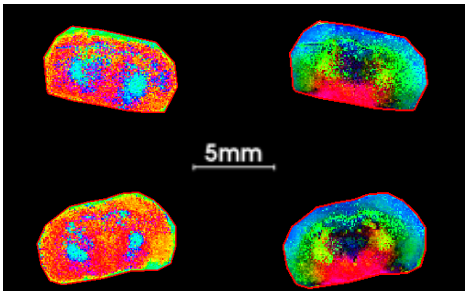


B **5 phospholipids (-PEs)**

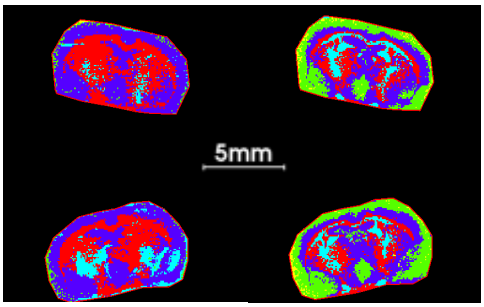


**Ratio:** - + - +

# Figure 7

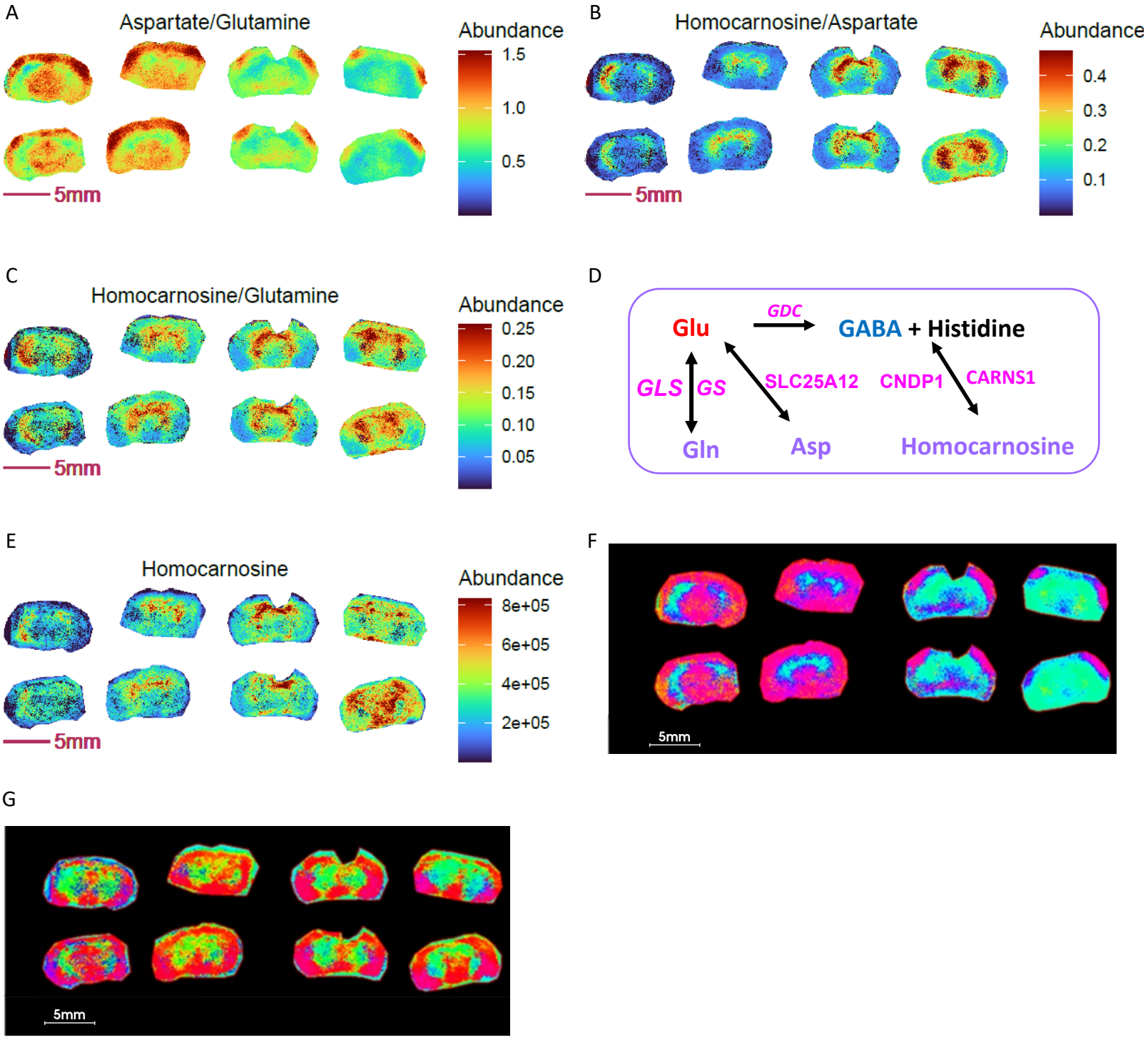
A
Aspartate/Glutamine
Abundance
1.5
1.0
0.5
5mm
B
Homocarnosine/Aspartate
Abundance
0.4
0.3
0.2
0.1
5mm
C
Homocarnosine/Glutamine
Abundance
0.25
0.20
0.15
0.10
0.05
5mm
D
Glu
GDC
GABA + Histidine
GLS
GS
SLC25A12
CNDP1
CARNS1
Gln
Asp
Homocarnosine
E
Homocarnosine
Abundance
8e+05
6e+05
4e+05
2e+05
5mm
F
5mm
G
5mm

**Figure 8**

A

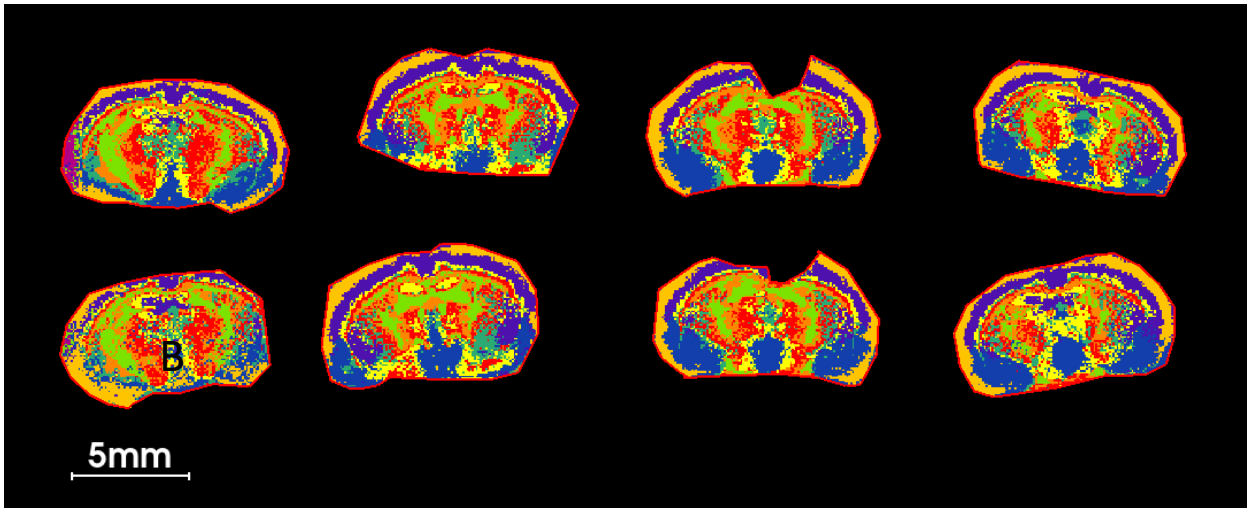


B

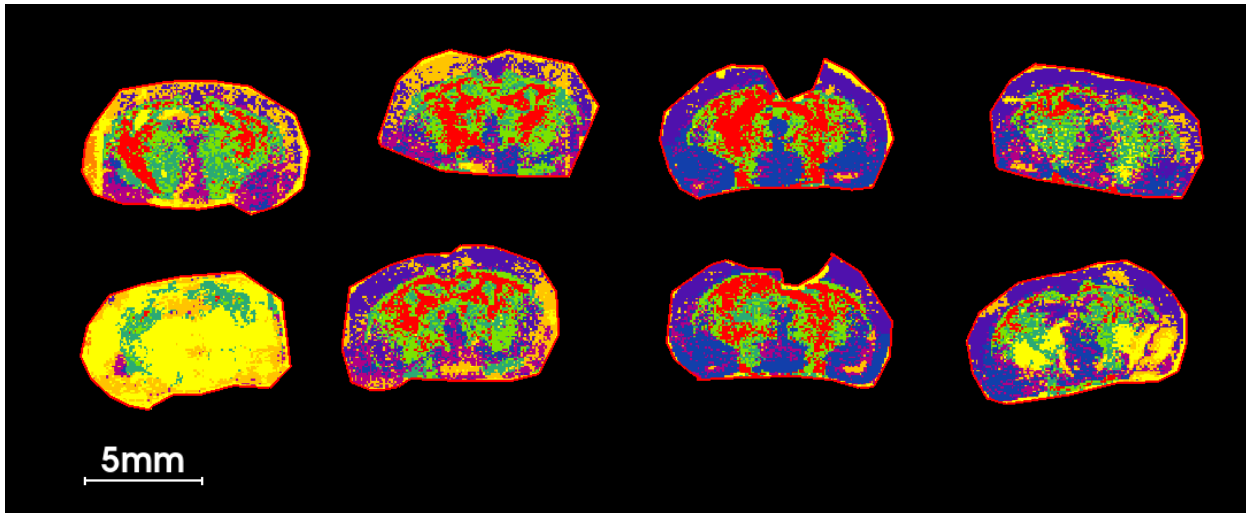

# Figure S1

A

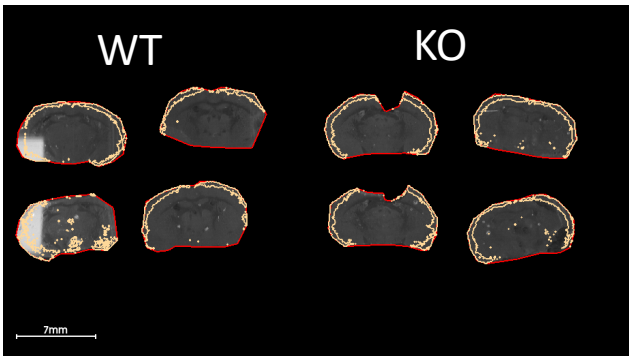


B

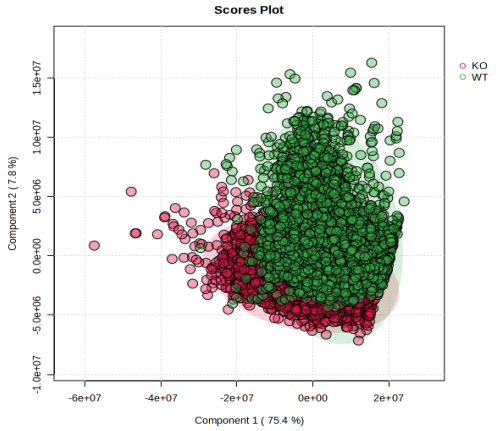


C

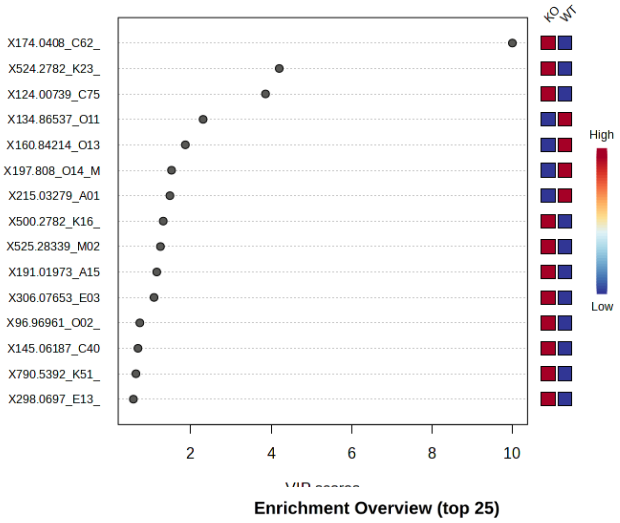


D

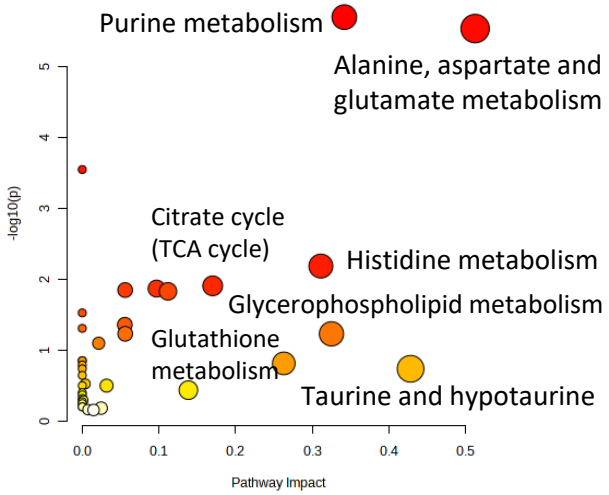


E

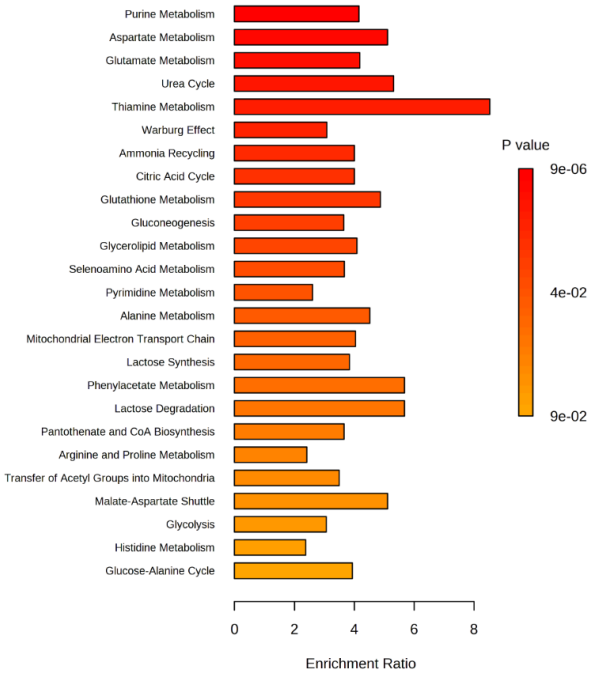


F

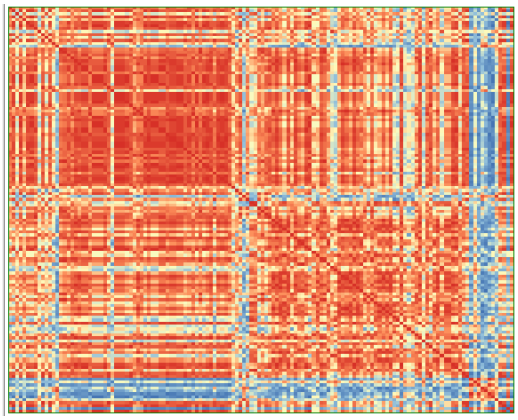

# Figure S2

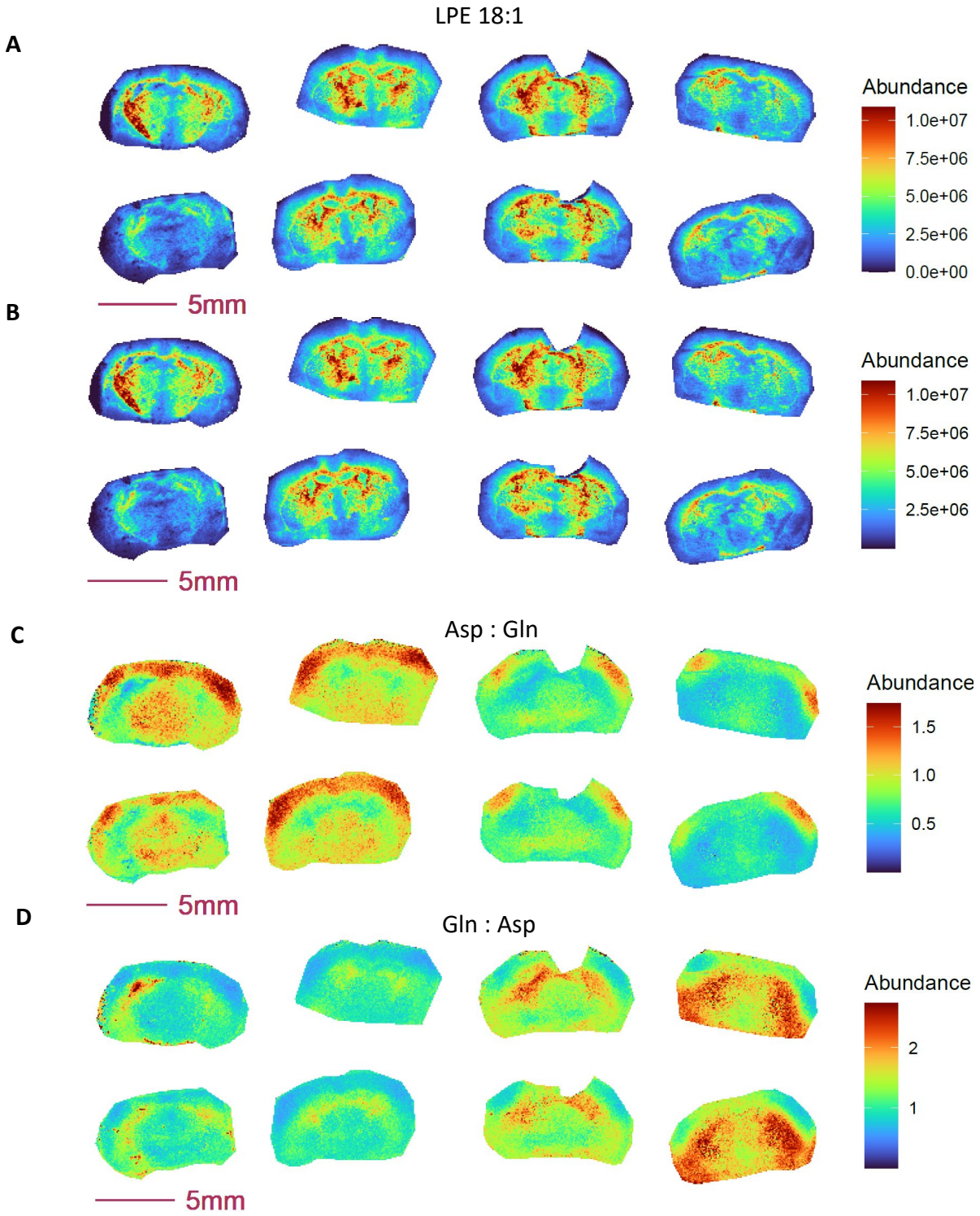
LPE 18:1
A
Abundance
1.0e+07
7.5e+06
5.0e+06
2.5e+06
0.0e+00
5mm
B
Abundance
1.0e+07
7.5e+06
5.0e+06
2.5e+06
5mm
C
Asp : Gln
Abundance
1.5
1.0
0.5
5mm
D
Gln : Asp
Abundance
2
1
5mm

# Figure S3

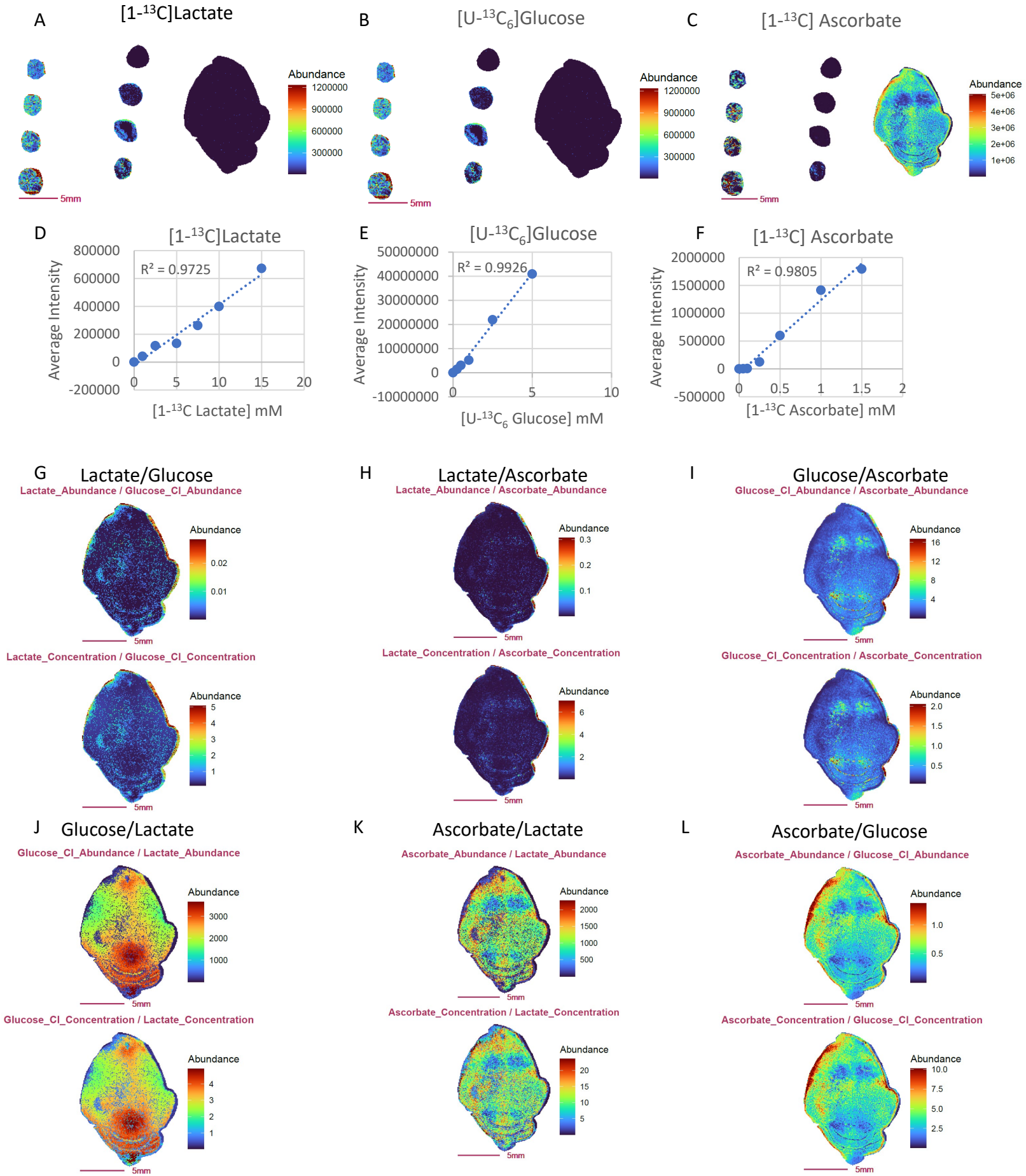
A
[1-13C]Lactate
Abundance
1200000
900000
600000
300000
5mm
B
[U-13C6]Glucose
Abundance
1200000
900000
600000
300000
5mm
C
[1-13C] Ascorbate
Abundance
5e+06
4e+06
3e+06
2e+06
1e+06
5mm
D
[1-13C]Lactate
R² = 0.9725
Average Intensity
800000
600000
400000
200000
0
-200000
0
5
10
15
20
[1-13C Lactate] mM
E
[U-13C6]Glucose
R² = 0.9926
Average Intensity
50000000
40000000
30000000
20000000
10000000
0
-10000000
0
5
10
[U-13C6 Glucose] mM
F
[1-13C] Ascorbate
R² = 0.9805
Average Intensity
2000000
1500000
1000000
500000
0
-500000
0
0.5
1
1.5
2
[1-13C Ascorbate] mM
G
Lactate/Glucose
Lactate_Abundance / Glucose_Cl_Abundance
Abundance
0.02
0.01
5mm
Lactate_Concentration / Glucose_Cl_Concentration
Abundance
5
4
3
2
1
5mm
H
Lactate/Ascorbate
Lactate_Abundance / Ascorbate_Abundance
Abundance
0.3
0.2
0.1
5mm
Lactate_Concentration / Ascorbate_Concentration
Abundance
6
4
2
5mm
I
Glucose/Ascorbate
Glucose_Cl_Abundance / Ascorbate_Abundance
Abundance
16
12
8
4
5mm
Glucose_Cl_Concentration / Ascorbate_Concentration
Abundance
2.0
1.5
1.0
0.5
5mm
J
Glucose/Lactate
Glucose_Cl_Abundance / Lactate_Abundance
Abundance
3000
2000
1000
5mm
Glucose_Cl_Concentration / Lactate_Concentration
Abundance
4
3
2
1
5mm
K
Ascorbate/Lactate
Ascorbate_Abundance / Lactate_Abundance
Abundance
2000
1500
1000
500
5mm
Ascorbate_Concentration / Lactate_Concentration
Abundance
20
15
10
5
5mm
L
Ascorbate/Glucose
Ascorbate_Abundance / Glucose_Cl_Abundance
Abundance
1.0
0.5
5mm
Ascorbate_Concentration / Glucose_Cl_Concentration
Abundance
10.0
7.5
5.0
2.5
5mm

**Figure S4**

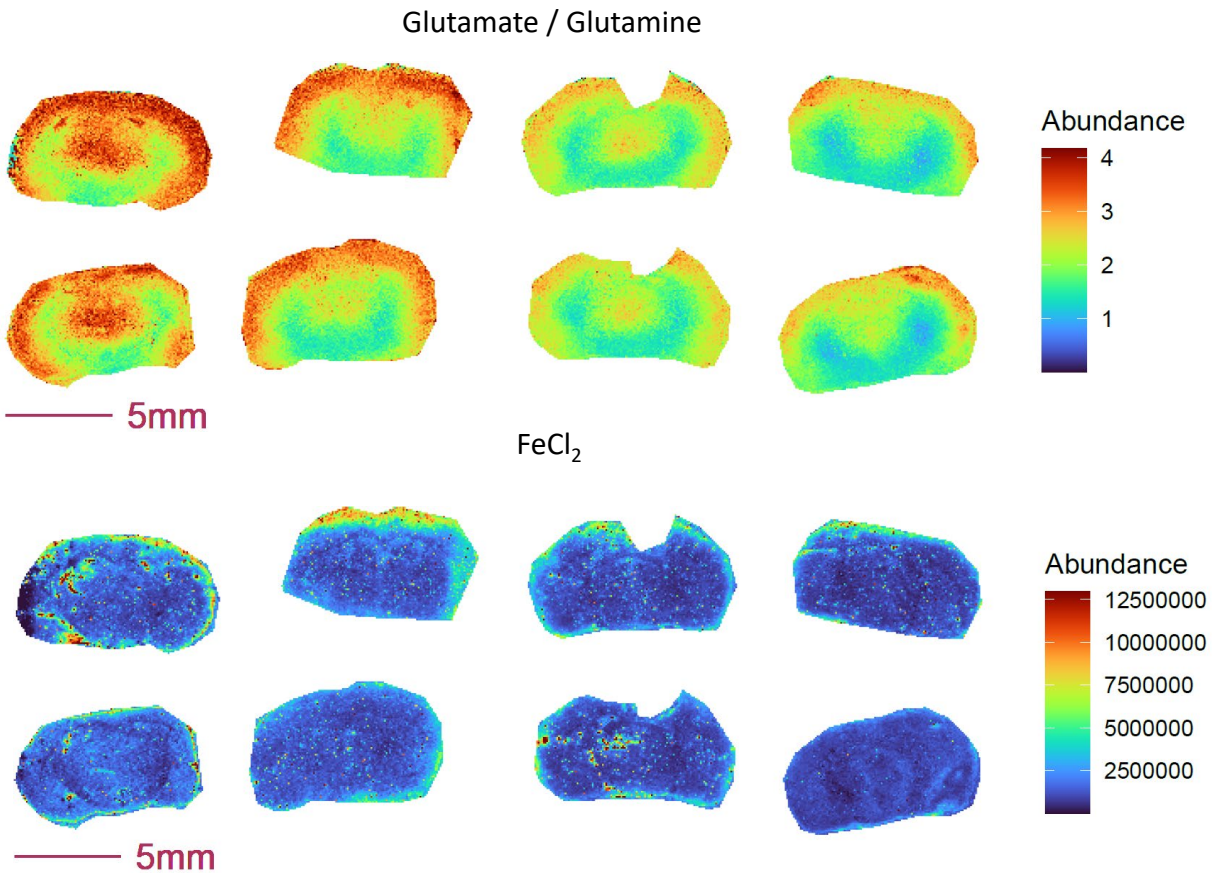
Glutamate / Glutamine
Abundance
4
3
2
1
5mm
FeCl2
Abundance
12500000
10000000
7500000
5000000
2500000
5mm

# Figure S5

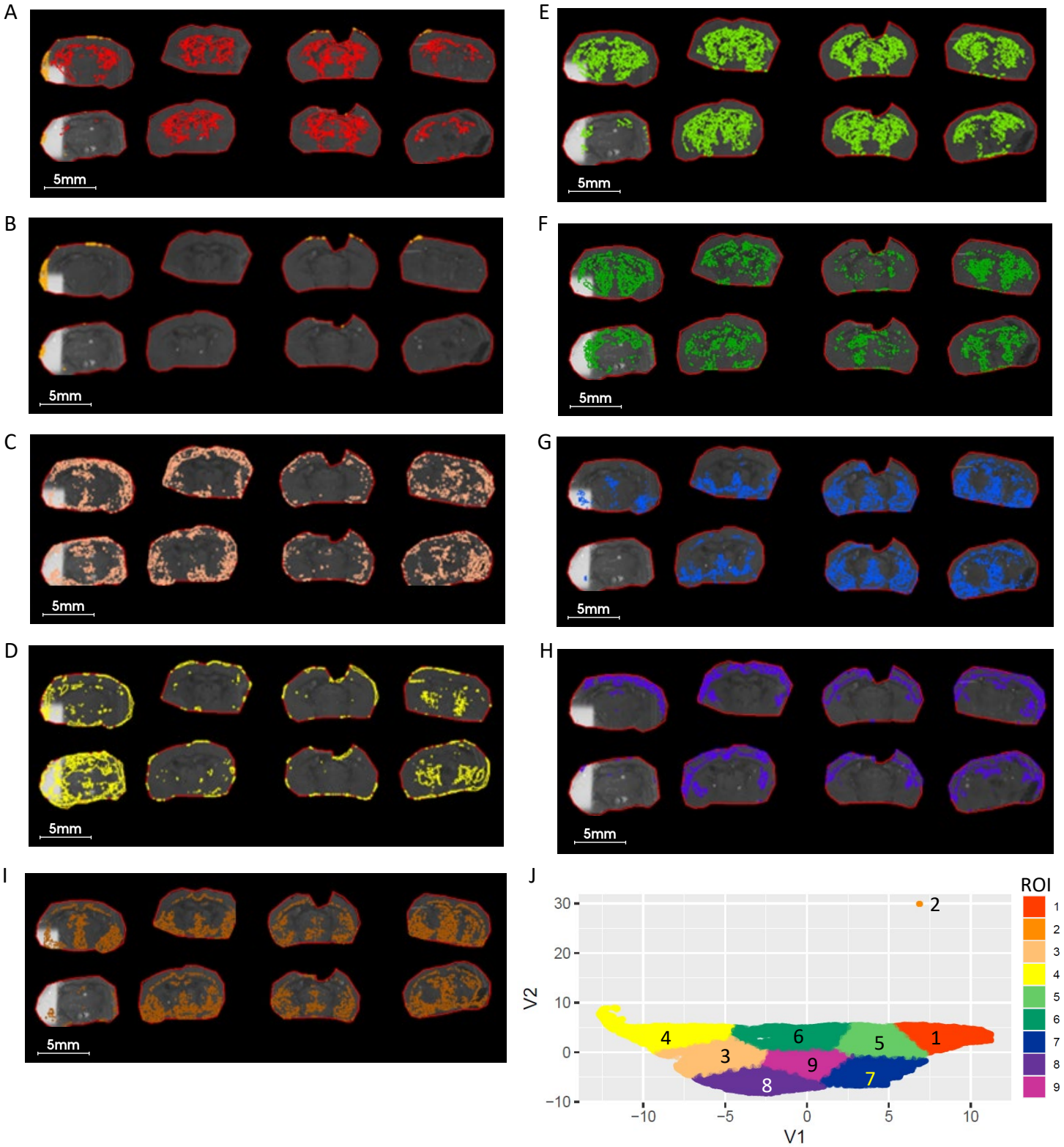

# Figure S6

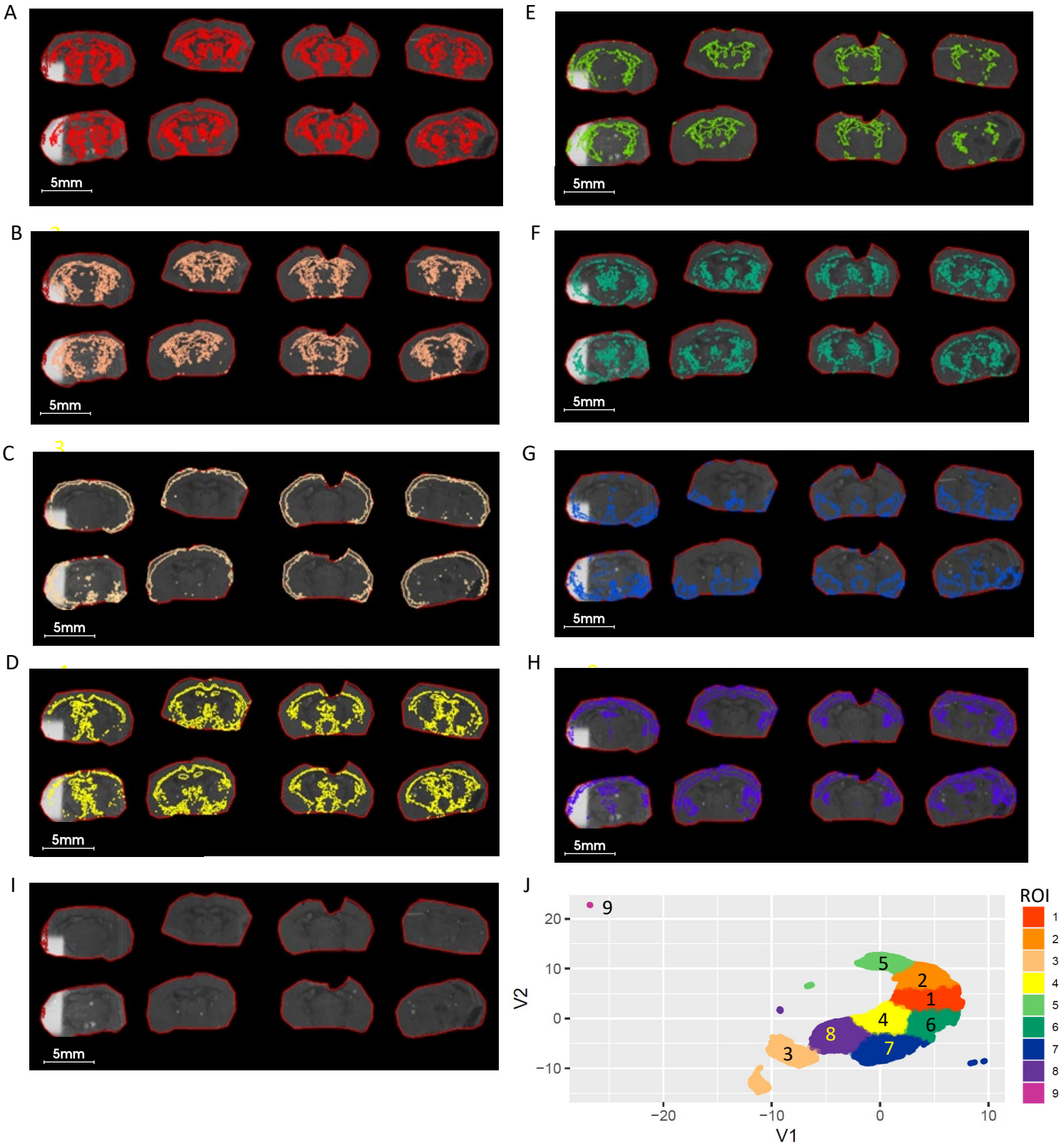

# Figure S7

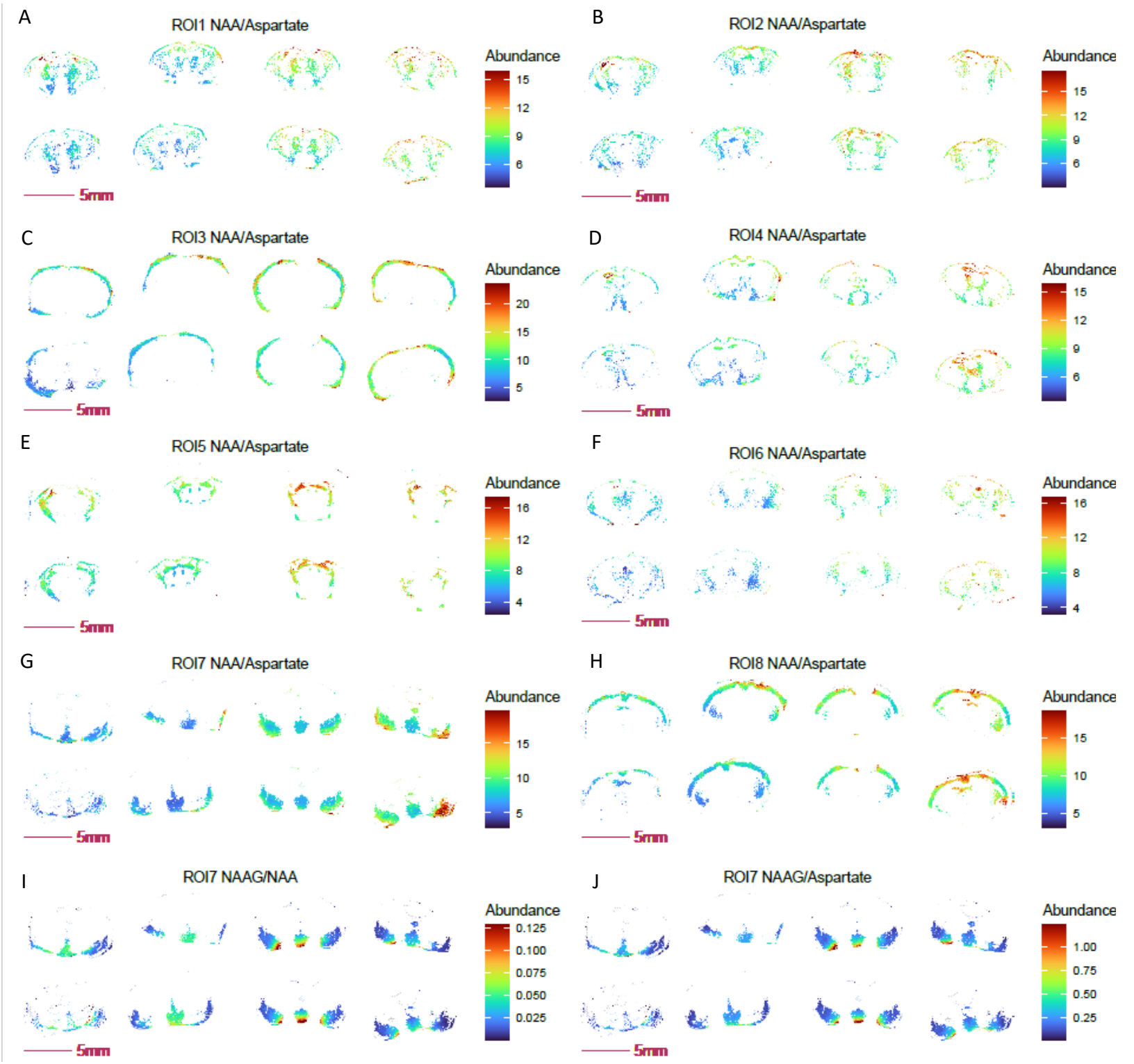
A
ROI1 NAA/Aspartate
Abundance
15
12
9
6
5mm
B
ROI2 NAA/Aspartate
Abundance
15
12
9
6
5mm
C
ROI3 NAA/Aspartate
Abundance
20
15
10
5
5mm
D
ROI4 NAA/Aspartate
Abundance
15
12
9
6
5mm
E
ROI5 NAA/Aspartate
Abundance
16
12
8
4
5mm
F
ROI6 NAA/Aspartate
Abundance
16
12
8
4
5mm
G
ROI7 NAA/Aspartate
Abundance
15
10
5
5mm
H
ROI8 NAA/Aspartate
Abundance
15
10
5
5mm
I
ROI7 NAAG/NAA
Abundance
0.125
0.100
0.075
0.050
0.025
5mm
J
ROI7 NAAG/Aspartate
Abundance
1.00
0.75
0.50
0.25
5mm

# Figure S8

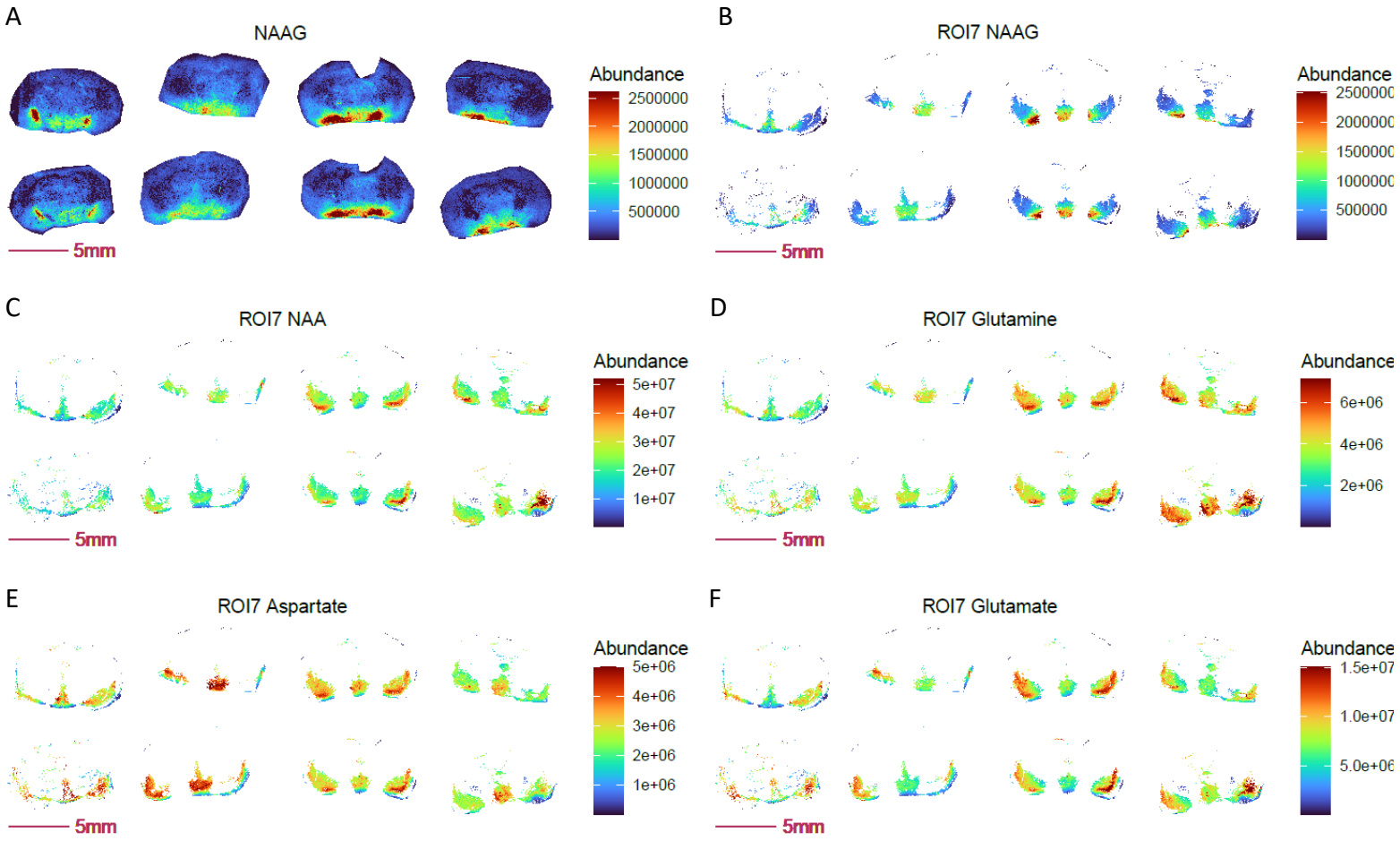
A
NAAG
Abundance
2500000
2000000
1500000
1000000
500000
5mm
B
ROI7 NAAG
Abundance
2500000
2000000
1500000
1000000
500000
5mm
C
ROI7 NAA
Abundance
5e+07
4e+07
3e+07
2e+07
1e+07
5mm
D
ROI7 Glutamine
Abundance
6e+06
4e+06
2e+06
5mm
E
ROI7 Aspartate
Abundance
5e+06
4e+06
3e+06
2e+06
1e+06
5mm
F
ROI7 Glutamate
Abundance
1.5e+07
1.0e+07
5.0e+06
5mm

# Figure S9

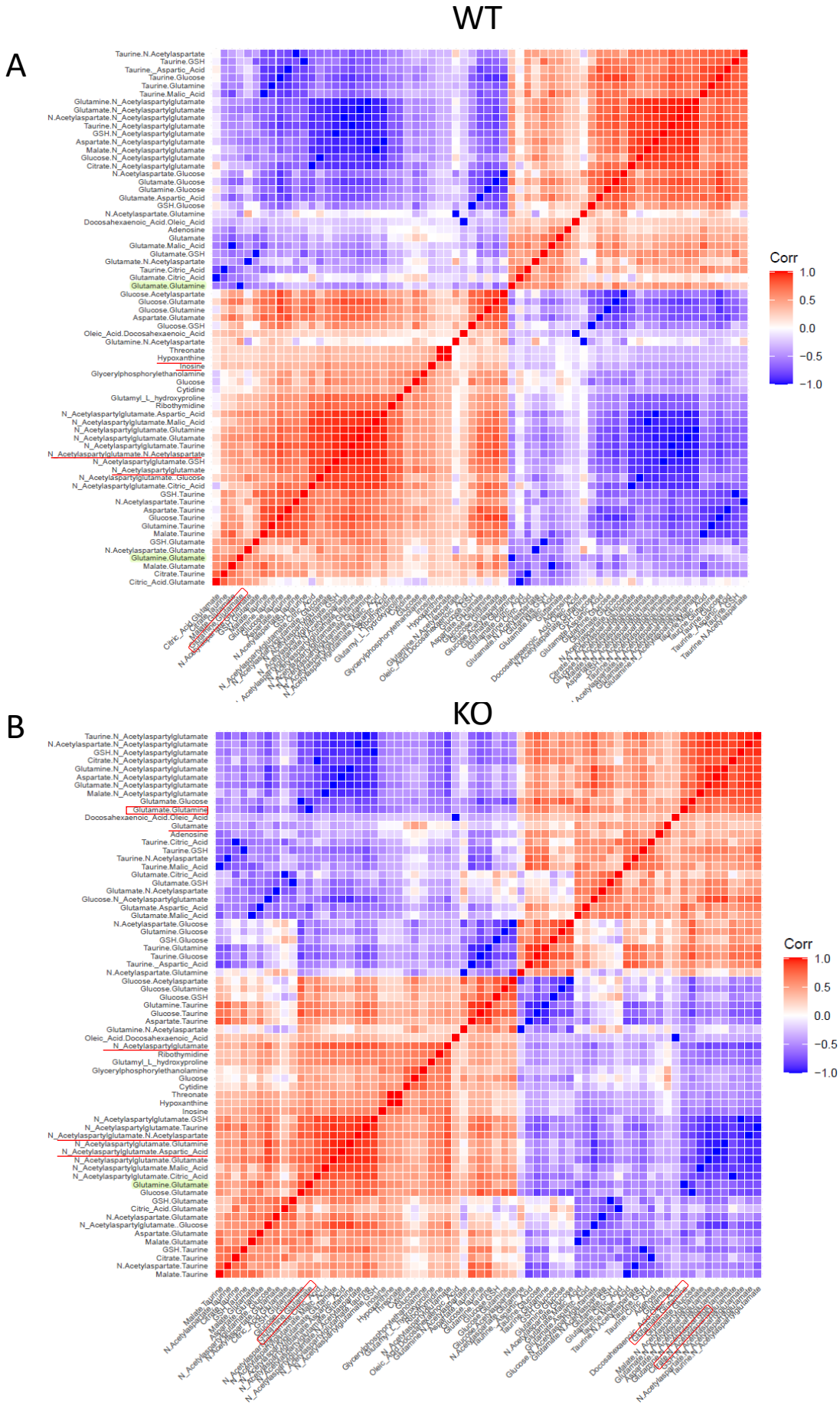

# Figure S10

A

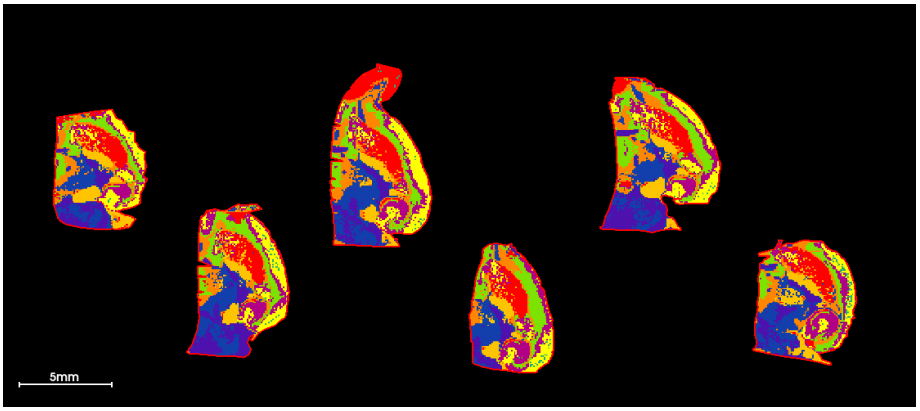


B

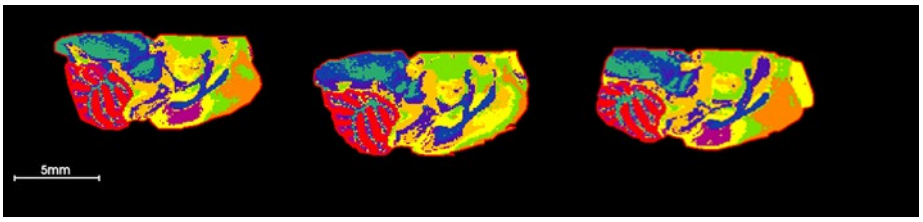


C

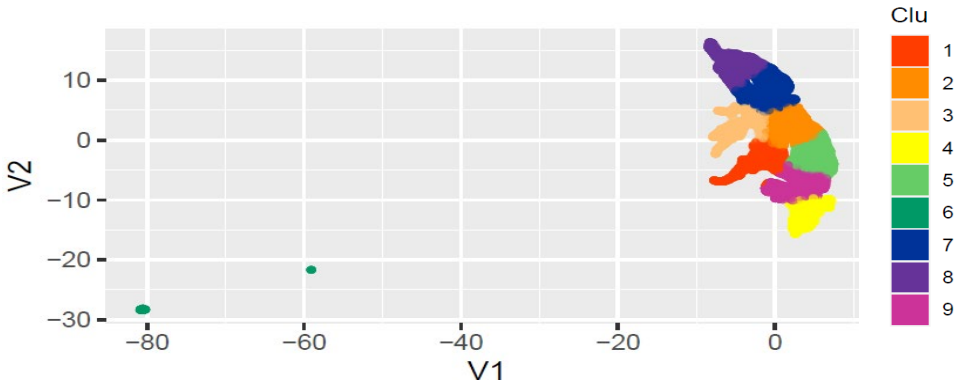


D

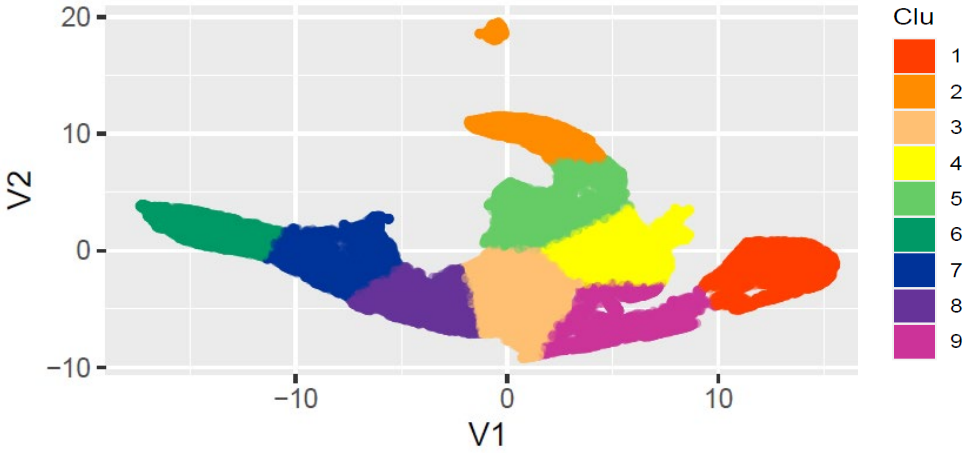

**Table1** Spearman correlation of an unknown with ratio and non-ratio entities

| Entity | Unknown [M-H] 375 23059 |
|---|---|
| CPA 18:1 | 0 86090633 |
| CPA 16:0 | 0 85862853 |
| Docosahexaenoic_Acid | 0 84761078 |
| Palmitic_Acid | 0 80091519 |
| LPA 18:1 | 0 78455912 |
| LPA 16:0 | 0 77663768 |
| Oleic_Acid | 0 77371792 |
| PA 34:2 | 0 73231961 |
| PA 36:3 | 0 72919804 |
| Palmitoleic_Acid | 0 72724047 |
| CPA 18:0 | 0 70128825 |
| LPE 16:0 | 0 69156441 |
| PA 38:6 | 0 68799022 |
| LPA 18:0 | 0 67264794 |
| 558. 4283 | 0 67163649 |
| PE P 16:0 | 0 66456185 |
| Linoleic_Acid | 0 65773742 |
| PI 36:2 | 0 65460109 |
| LPA 18:2 / LPA 18:1 | -0 53780801 |
| PA 36:1 / LPA 18:1 | -0 4549225 |
| PA 36:4 /  LPA 16:0 | -0 42353603 |

**Table 2** Brain glutamate to glutamine ratio positively correlates $FeCl_2$ using combined ratio and non-ratio pixel data and spearman correlation

| Metabolite or Metabolite ratio | Gltamate / Glutamine |
|---|---|
| Glutamate / Glutamine | 1 |
| N-Acetylaspartate / Glutamine | 0.69140746 |
| Glutamate / Glucose | 0.68318508 |
| Aspartate / Glutamine | 0.617246741 |
| Aspartate / Glucose | 0.571634522 |
| N-Acetylaspartate / Glucose | 0.487447557 |
| Glutathione / Glutamine | 0.482704981 |
| Glutamate / Malate | 0.477826203 |
| Glutamate / NAAG | 0.418208761 |
| Glutathione / Glucose | 0.414914055 |
| Glutamate / Taurine | 0.408270132 |
| Aspartate / NAAG | 0.40560898 |
| $FeCl_2$ | 0.40137113 |

**Table S1** Comparison of untargeted ratio imaging R workflow to other ratio software

| Ratio image tools | MSI specific software | Workable Image Data Format | Targeted input Ratio image | Untargeted ratio image | Free and open source |
|---|---|---|---|---|---|
| R workflow | Yes | Excel, imzml | yes | yes | yes |
| ENVI IDL | No | Optical and SAR Data | yes | no | no |
| MATLAB RatioImage App | No | Variety files including Image, Text, Spreadsheet, MATLAB data file | yes | no | no |
| Spectral Python package | No | ENVI, AVIRIS, ERDAS/Lan, imzml | yes | no | yes |
| QGIS hyperspectral image analysis | No | Image, Text, StreetMap, PostGIS etc | yes | no | yes |

**Table S2** Brain glutamine to glutamate ratio negatively correlates $FeCl_2$ using combined ratio and non-ratio pixel data and spearman correlation

| Metabolte or Metabolite ratio | Glutamine /Glutamate |
|---|---|
| Glutamine / Glutamate | 1 |
| NAA / Glutamine | -0.691412587 |
| Glutamate / Glucose | -0.683182994 |
| Aspartate / Glutamine | -0.617245759 |
| Aspartate / Glucose | -0.571635589 |
| NAA / Glucose | -0.48745363 |
| Glutathione / Glutamine | -0.482699341 |
| Glutamate / Malate | -0.477828273 |
| Glutamate / NAAG | -0.418214673 |
| Glutathione / Glucose | -0.414916374 |
| Glutamate / Taurine | -0.408268788 |
| Aspartate / NAAG | -0.40561461 |
| $FeCl_2$ | -0.40137478 |

**Table S3** list of glutamate metabolism related metabolites for ratio generation and PCA segmentation of brain sections

| m/z | Name |
|---|---|
| 215.03279 | Glucose+Cl |
| 191.01973 | Citrate |
| 133.01425 | Malate |
| 132.03023 | Aspartate |
| 146.04588 | Glutamate |
| 145.06187 | Glutamine |
| 174.0408 | N-Acetylaspartate |
| 303.08339 | N-Acetylaspartylglutamate |
| 124.00739 | Taurine |
| 306.07653 | Glutathione |

**Table S4** list of lyso PEs for ratio generation and PCA segmentation of brain sections

| m/z | Name |
|---|---|
| 478.2939 | LPE 18:1 |
| 506.3252 | LPE 20:1 |
| 500.2782 | LPE 20:4 |
| 528.3095 | LPE 22:4 |
| 524.2782 | LPE 22:6 |

**Table S5** Comparing correlation of neurotransmitter related metabolites and ratios in ROI7 of WT and KO brains

| Entity Name | Spearman R square (WT) | Spearman R square (KO) |
|---|---|---|
| Glutamate/Glutamine | 1 | 1 |
| Glutamate/Glucose | 0.852795869 | 0.678393963 |
| Glutamate/Aspartic acid | 0.801507737 | 0.558480678 |
| Glutamate/N_Acetylaspartylglutamate | 0.800125626 | 0.597592592 |
| N_Acetylaspartate/N_Acetylaspartylglutamate | 0.759938917 | 0.543231796 |
| Taurine/N_Acetylaspartylglutamate | 0.747279077 | 0.493250032 |
| GSH/N_Acetylaspartylglutamate | 0.725654702 | 0.534683985 |
| Citrate/N_Acetylaspartylglutamate | 0.670060429 | 0.3079266 |
| Aspartate/N_Acetylaspartylglutamate | 0.659178165 | 0.568779025 |
| Glutamate/Malic acid | 0.65035649 | 0.666255195 |
| Taurine/Glutamine | 0.648921859 | 0.554419257 |
| Taurine/Glucose | 0.644297546 | 0.452028615 |
| Glutamine/N_Acetylaspartylglutamate | 0.643225848 | 0.436576981 |
| Malate/N_Acetylaspartylglutamate | 0.624522126 | 0.441813603 |
| Glutamate/N-Acetylaspartate | 0.603496857 | 0.536109488 |
| Glutamate/GSH | 0.592151602 | 0.531586301 |
| Taurine/GSH | 0.567926578 | 0.282270798 |
| Taurine/Malic acid | 0.561595842 | 0.437632948 |
| Glucose/N_Acetylaspartylglutamate | 0.546762829 | 0.456179028 |
| Taurine/Aspartate | 0.543991912 | 0.289845889 |
| N-Acetylaspartate/Glucose | 0.485692311 | 0.460863975 |
| Adenosine | 0.48250312 | 0.339646908 |
| Taurine/N-Acetylaspartate | 0.480117014 | 0.263254553 |
| Taurine/Citrate | 0.444918698 | 0.56298861 |
| Glutamine/Glucose | 0.431762837 | 0.252386832 |
| Glutamate | 0.427270886 | 0.528188618 |
| Glutamate/Citrate | 0.414241714 | 0.592641696 |
| Docosahexaenoic acid/Oleic acid | 0.412424989 | 0.316780465 |
| GSH/Glucose | 0.409754542 | 0.418037354 |
| N-Acetylaspartate/Glutamine | 0.402130321 | 0.503623165 |
| Glutamine/N-Acetylaspartate | -0.402121379 | -0.503623105 |
| Glucose/GSH | -0.409720091 | -0.418038021 |
| Oleic acid/Docosahexaenoic acid | -0.412418152 | -0.316772044 |
| Citrate/Glutamate | -0.41420686 | -0.592642619 |
| Glucose | -0.414832304 | -0.247192996 |
| Glucose/Glutamine | -0.431769617 | -0.252433325 |
| Cytidine | -0.440811865 | -0.091933842 |
| Citrate/Taurine | -0.444846276 | -0.562985142 |
| Glycerylphosphorylethanolamine | -0.446969716 | -0.132695491 |
| N-Acetylaspartate/Taurine | -0.480131641 | -0.263259877 |
| Glucose/Acetylaspartate | -0.485566843 | -0.460873356 |
| Aspartate/Taurine | -0.543994549 | -0.2898528 |
| N_Acetylaspartylglutamate//Glucose | -0.546773877 | -0.456197823 |
| Ribothymidine | -0.553276958 | -0.345023745 |
| Hypoxanthine | -0.55899857 | -0.220084088 |
| Threonate | -0.559486345 | -0.21885935 |
| Malate/Taurine | -0.56159942 | -0.437638439 |
| GSH/Taurine | -0.56793975 | -0.28227912 |
| Glutamyl_L_hydroxyproline | -0.576156273 | -0.366588722 |
| GSH/Glutamate | -0.592167807 | -0.531584116 |
| N-Acetylaspartate/Glutamate | -0.603520459 | -0.536111131 |
| N_Acetylaspartylglutamate/Malic acid | -0.624526454 | -0.441825388 |
| N_Acetylaspartylglutamate/Glutamine | -0.643220125 | -0.43659667 |
| Glucose/Taurine | -0.644270344 | -0.452036941 |
| Glutamine/Taurine | -0.64890671 | -0.554426135 |
| Malate/Glutamate | -0.650339314 | -0.666263387 |
| Inosine | -0.652470417 | -0.328246954 |
| **N_Acetylaspartylglutamate** | **-0.657380577** | **-0.463920793** |
| **N_Acetylaspartylglutamate/Aspartic acid** | **-0.659182447** | **-0.568791965** |
| N_Acetylaspartylglutamate/Citrate | -0.670054261 | -0.307934844 |
| N_Acetylaspartylglutamate/GSH | -0.725656919 | -0.53469776 |
| N_Acetylaspartylglutamate/Taurine | -0.747279393 | -0.493256641 |
| **N_Acetylaspartylglutamate/N-Acetylaspartate** | **-0.759938281** | **-0.543230626** |
| N_Acetylaspartylglutamate/Glutamate | -0.800114153 | -0.59760264 |
| Aspartate/Glutamate | -0.80148754 | -0.55847547 |
| Glucose/Glutamate | -0.852793526 | -0.678396625 |
| Glutamine/Glutamate | -0.999998899 | -0.999999747 |